**Atmospheric
Chemistry
and Physics**

Cluster analysis of midlatitude oceanic cloud regimes: mean properties and temperature sensitivity

N. D. Gordon[1,*] and J. R. Norris[1]

[1]Scripps Institution of Oceanography, University of California, San Diego La Jolla, CA, USA
[*]current address: School of Earth and Environment, University of Leeds Leeds, UK

Abstract. Clouds play an important role in the climate system by reducing the amount of shortwave radiation reaching the surface and the amount of longwave radiation escaping to space. Accurate simulation of clouds in computer models remains elusive, however, pointing to a lack of understanding of the connection between large-scale dynamics and cloud properties. This study uses a k-means clustering algorithm to group 21 years of satellite cloud data over midlatitude oceans into seven clusters, and demonstrates that the cloud clusters are associated with distinct large-scale dynamical conditions. Three clusters correspond to low-level cloud regimes with different cloud fraction and cumuliform or stratiform characteristics, but all occur under large-scale descent and a relatively dry free troposphere. Three clusters correspond to vertically extensive cloud regimes with tops in the middle or upper troposphere, and they differ according to the strength of large-scale ascent and enhancement of tropospheric temperature and humidity. The final cluster is associated with a lower troposphere that is dry and an upper troposphere that is moist and experiencing weak ascent and horizontal moist advection.

Since the present balance of reflection of shortwave and absorption of longwave radiation by clouds could change as the atmosphere warms from increasing anthropogenic greenhouse gases, we must also better understand how increasing temperature modifies cloud and radiative properties. We therefore undertake an observational analysis of how midlatitude oceanic clouds change with temperature when dynamical processes are held constant (i.e., partial derivative with respect to temperature). For each of the seven cloud regimes, we examine the difference in cloud and radiative properties between warm and cold subsets. To avoid misinterpreting a cloud response to large-scale dynamical forcing as a cloud response to temperature, we require horizontal and vertical temperature advection in the warm and cold subsets to have near-median values in three layers of the troposphere. Across all of the seven clusters, we find that cloud fraction is smaller and cloud optical thickness is mostly larger for the warm subset. Cloud-top pressure is higher for the three low-level cloud regimes and lower for the cirrus regime. The net upwelling radiation flux at the top of the atmosphere is larger for the warm subset in every cluster except cirrus, and larger when averaged over all clusters. This implies that the direct response of midlatitude oceanic clouds to increasing temperature acts as a negative feedback on the climate system. Note that the cloud response to atmospheric dynamical changes produced by global warming, which we do not consider in this study, may differ, and the total cloud feedback may be positive.

1 Introduction

Clouds play an integral role in the climate system by reflecting solar radiation back to space and restricting the emission of terrestrial radiation to space, thereby substantially influencing the Earth's temperature. For this reason, it is important to understand how clouds and their impacts on radiative transfer might respond to an initial warming from increased CO_2. This is known as the cloud-climate feedback. Although global climate models are commonly used to study climate change, there is currently no agreement between different models on the magnitude of the cloud-climate feedback, and the representation of clouds in climate models continues to

be the largest source of uncertainty in projections of future climate (IPCC, 2007).

Previous studies have used various compositing techniques to examine and compare how cloudiness is related to meteorological forcing in observations and models (e.g., Klein and Jakob, 1999; Norris and Weaver, 2001; Tselioudis and Jakob, 2002). Dividing the atmosphere into a series of distinct meteorological regimes, each with different cloud properties, is an effective method for understanding the connections between the dynamics and thermodynamics of the atmosphere and the clouds they produce (Jakob, 2003). More recent investigations have used clustering algorithms to more objectively identify cloud regimes without direct reference to meteorological parameters (e.g., Jakob and Tselioudis, 2003; Gordon et al., 2005; Jakob et al., 2005; Rossow et al., 2005). Williams and Tselioudis (2007) examined differences between simulated cloud properties in control runs and $2 \times CO_2$ experiments through the use of a clustering algorithm. Identifying the specific vertical distribution of dynamical and thermodynamical processes generating a particular type of cloud is crucial for understanding the atmosphere and improving model simulation of clouds.

The present study extends the clustering approach of Gordon et al. (2005) to all midlatitude ocean grid boxes, where clouds have a very large impact on shortwave radiation (Weaver and Ramanathan, 1997). Only ocean regions are examined so as to minimize the role that surface features play in cloud forcing. We use a k-means clustering algorithm to classify daily grid box cloud data from the International Satellite Cloud Climatology Project (ISCCP) into seven groups according to similar cloud fraction values in three cloud-top pressure intervals and three cloud optical thickness intervals. Vertical profiles of reanalysis relative humidity, temperature, vertical velocity, horizontal temperature advection, and horizontal moisture advection are averaged over each cluster as perturbations from the mean state. This provides insight into meteorological conditions and dynamical forcing associated with each cloud regime, which is supplemented by examination of the climatological distribution and seasonal cycle of each cluster.

Since current global climate models do not provide reliable information on the cloud response to global warming (e.g., Ringer et al., 2006; Clement et al., 2009; among others), we will additionally use our clustering analysis as a foundation for investigation of the sensitivity of cloud properties to changes in temperature. To avoid the confounding effects of dynamical processes that can influence both temperature and clouds, we investigate how cloud properties vary with temperature within a narrow range of dynamical parameters, following the approach of Bony et al. (2004). Clustering is a useful tool for this purpose because it groups cloud types with similar meteorology, and Williams and Tselioudis (2007) employed it to examine the relative contribution of changes to cloud properties due to dynamic and thermodynamic changes in GCMs. In the present study, each cluster is divided into relatively warm and cold subsets. The impact of joint dynamical forcing on temperature and cloudiness is removed by restricting warm and cold subsets to have near-median values of horizontal and vertical temperature advection and near-median values of lapse rate in the lower troposphere and tropopause region. The difference between cold and warm subsets provides information on how large-scale cloud and radiative properties are affected by increasing temperature directly rather than through changes in atmospheric circulation associated with global warming. These results will give insight into cloud feedback on the climate system and be a useful baseline for model evaluation.

2   Data sources

The source of cloud observations for this investigation was the three-hourly International Satellite Cloud Climatology Project (ISCCP) D1 equal-area ($280 \, km \times 280 \, km$) data set, originally processed from radiances primarily measured by geostationary weather satellites (Rossow et al., 1996; Rossow and Schiffer, 1999). The ISCCP data consist of cloud fractions within a grid box for nine categories of cloudiness based on three intervals of cloud-top pressure (CTP) (below 680 mb, between 680 and 440 mb, and above 440 mb) and three intervals of cloud optical thickness (τ) (between 0.3 and 3.6, between 3.6 and 23, and above 23). Satellite pixels used to generate the CTP-τ histograms are approximately 4–7 km in size and spaced approximately 30 km apart, with up to 80 pixels per grid box. Since cloud optical thickness values are obtained from visible retrievals, valid data only exist for daytime hours. We restricted our analysis to one time point per day for each satellite grid box, choosing the value with the smallest solar-zenith angle (closest to local noon). This restriction avoided sampling biases associated with more valid data points coming from regions near the equator and from points in the summer hemisphere, where there are a greater number of daylight hours.

Additional quality control included removal of all grid box values with any sea ice, as reported by the satellite, or any points with anomalously high clear-sky albedo (α_{clear}). The normal range of α_{clear} was determined for bins of solar-zenith angle (SZA) by calculating the difference between the first percentile and the median value. For each SZA bin, all data for which α_{clear} values were greater than the sum of the median and the difference between the median and the first percentile value were excluded. This assumes that valid α_{clear} varies uniformly above and below the median. We also excluded data for which satellite skin temperature (T_{skin}) was less than 271 K, more than 4 K colder than NCEP reanalysis SST, or more than 8 K warmer than reanalysis SST. As noted by Tsuang et al. (their Fig. 3, 2008), T_{skin} tended to be warmer than NCEP reanalysis SST by about 2 K for most observations over the midlatitude oceans. All of these restrictions removed less than 1% of the initial data, but it

was necessary to ensure that spurious clear-sky values did not contaminate our analysis of changes in cloud radiative properties.

Our analysis spans nearly the entire available record of ISCCP, 21 years (1984–2004), and incorporates all ocean points between 30° and 55° in both hemispheres, representing 1444 grid boxes. The ISCCP data consisted of nearly 10 million CTP-τ histograms over all days and grid boxes, thus enabling a comprehensive investigation of the cloud response to temperature when large-scale dynamical conditions are held constant. The CTP-τ histogram corresponds to a nine-type cloud fraction array. All values of the nine-type cloud fraction array are exactly zero for clear-sky observations, which infrequently occur (less than 1% of the total number of days and grid boxes) and are excluded from the clustering. To complement the satellite-derived properties of the cloud regimes, we also analyzed surface-based visual cloud type observations from the Extended Edited Cloud Report Archive (EECRA) (Hahn and Warren, 1999).

In addition to mean cloud properties, we examined the three-hourly radiative flux data derived from the ISCCP data (Zhang et al., 2004). The flux data consists of upwelling and downwelling, shortwave and longwave radiative flux for both clear and cloudy parts of the grid box. This data is provided at the surface, the top of the atmosphere (TOA), and at three levels within the atmosphere (680 mbar, 440 mbar, and 100 mbar). While the uncertainties of instantaneous flux values are on the order of $10 \, \text{Wm}^2$, these will be considerably reduced in the clusters by averaging over a large number of values. While systematic biases may exist in ISCCP FD data due to satellite changes, we do not expect them to produce substantial differences between cloud clusters.

Since our selection of the one satellite observation per day that is closest to local noon would otherwise produce a substantial radiative bias, we divided near-noon upwelling TOA SW fluxes by near-noon insolation to convert them to values of reflectivity. Reflectivity values were multiplied by diurnal mean insolation to convert them back to diurnal mean upwelling SW flux (more details are available in Appendix A). This procedure assumes that systematic cloud changes near local noon are characteristic of the entire day. Averaging diurnal mean flux values across different grid boxes and seasons gives more radiative weighting to cloud changes that occur at lower latitudes and during the summer season. While this may be more relevant to the overall impact on climate, in the present study we are more interested in the typical cloud response to increasing temperature. For this reason we gave equal weighting to clouds in all grid boxes and seasons by separately averaging reflectivity values and diurnal mean insolation values before multiplying them together to obtain average diurnal mean upwelling flux. Our results are qualitatively the same irrespective of radiative weighting.

We obtained information about the dynamics and thermodynamic structure of the atmosphere from the National Center for Environmental Prediction (NCEP) NCAR Reanalysis (Kalnay et al., 1996). This data set provided standard meteorological parameters as well as information about large-scale gradients and atmospheric motions that were needed to calculate the advective tendencies of moisture and temperature, which are important to cloud formation and dissipation. We have restricted our analysis to middle latitudes because that is where much of the dynamical forcing that leads to cloud formation in these regions is at or above the spatial scale of the satellite grid boxes. Moreover, vertical motion at middle latitudes is better constrained via quasi-geostrophic relationships by satellite and radiosonde observations of temperature and horizontal wind. Although deficiencies exist in the dynamics as represented in reanalyses (Trenberth et al., 2001), the accuracy of the NCEP Reanalysis in the midlatitudes is greatly improved in the model satellite era, post 1978 (Bromwich and Fogt, 2004). Additionally, our main interest is in the relationship between dynamics and cloud properties, and Norris and Weaver (2001) found negligible differences between cloud-vertical motion relationships when using the NCEP and ECMWF Reanalyses.

3 Cluster analysis method

The ISCCP cloud data were grouped into regimes by applying a k-means clustering algorithm to the nine-type cloud fraction arrays (CTP-τ histograms). The k-means procedure classifies all nine-type arrays into a specified number of clusters such that within-cluster variance is minimized (Hartigan, 1975; Jakob and Tselioudis, 2003). The only arbitrary parameter needed is the number of clusters; the character of the individual cluster means is then objectively determined by the data. The clustering process began with random selection of k nine-type arrays as initial seeds. All other nine-type arrays in the data set were then assigned to the initial seed to which they were closest in a Euclidean sense. The number of nine-type arrays in a cluster divided by the total number of nine-type arrays is the frequency of occurrence of the cluster, and the average of all nine-type arrays in the cluster is the centroid (i.e., average cloud fraction for each of the nine CTP-τ categories). These cluster centroids became new seeds to reinitialize the clustering routine, which was repeated until the centroids converged.

An uncertainty in the k-means method is the convergence of the clustering algorithm to different results for different initial seeds. We resolved this ambiguity by clustering on 50 different sets of random initial seeds and choosing the final cluster set with the least sum of variance around each cluster centroid (the other possible solutions will be discussed later). Specifying the number of clusters is the most subjective aspect of the k-means method. After examining results for various numbers, we chose to use seven clusters, as that was the minimum number of clusters that had clearly distinct cloud properties and meteorological conditions. Additional clusters beyond seven exhibited great similarity to one of the

Table 1. Grid box mean ISCCP cloud properties for each cluster.

	1 – Small Cu	2 – Large Cu	3 – Sc/St	4 – Deep As	5 – Cirrus	6 – Weak Frontal	7 – Strong Frontal
Cluster Frequency (%)	27.5	18.4	16.5	14.0	11.3	7.7	4.3
Mean Cloud Fraction (%)	54.1	77.8	92.9	97.5	87.4	99.0	99.4
Mean Cloud-Top Pressure (mb)	658.2	781.0	776.4	584.3	431.8	382.6	347.6
Mean Cloud Optical Thickness	3.63	2.89	7.19	8.30	2.30	8.90	23.08

preceding clusters without providing appreciable new information; inclusion of such intermediate clusters would have increased the number of plots without commensurately enhancing our understanding of dynamical and thermodynamical conditions associated with particular cloud regimes.

Our approach differs from that of Gordon et al. (2005) in that we cluster on cloud fraction in nine CTP-τ categories rather than grid box mean cloud fraction, cloud-top pressure, and cloud reflectivity. We instead took the approach used by Jakob and Tselioudis (2003), except that they used 42 CTP-τ categories (cloud fraction within each of seven CTP and six τ intervals). Because cloud fraction in 42 CTP-τ categories did not provide significantly more information, we aggregated the 42 categories into nine categories that correspond to the standard ISCCP-defined cloud types.

4 Cloud properties

Table 1 lists mean cloud fraction, CTP and τ averaged over all CTP-τ categories for the cluster centroids during the 1984–2004 time period, ordered according to relative frequency. The nonlinear relationship between radiation flux and optical thickness was taken into account by converting cloud optical thickness values to cloud reflectivity at 0.6 microns using an ISCCP look-up table (corresponding to Fig. 3.13 in Rossow et al., 1996) before averaging. The mean reflectivity was then converted back to cloud optical thickness using the same table. This ensures that our cluster mean optical thickness values more correctly represent cloud effects on grid box mean visible radiation flux.

Table 2 lists mean TOA shortwave cloud radiative forcing (SWCRF) and longwave cloud radiative forcing (LWCRF) for each of the clusters. These are diurnal mean values calculated from near-noon values according to the method described in the Appendix. Following Charlock and Ramanathan (1985), we define cloud radiative forcing as outgoing radiative flux for all-sky conditions subtracted from outgoing radiative flux for cloud-free conditions. Thus, SWCRF values are negative and represent a net cooling of the climate system, and LWCRF values are positive and represent a net warming of the climate system. Reasons for the informal

names given to each cluster in Tables 1 and 2 will be described in the following paragraphs.

As a complement to the satellite observations, we examined cloud information reported by surface observers on ships in the same grid box and on the same day as the ISCCP data. These provide a bottom-up view of the scene along with morphological rather than radiative characterizations of cloud types as well as precipitation (see Table 1 of Norris, 1998a). Table 3 lists average surface-observed total cloud cover and low-level cloud cover for each cluster together with the frequencies at which surface observers report the occurrence of clear sky, sky obscuration by fog or precipitation, non-drizzle precipitation, various low-level cloud types, and the absence of low-level cloudiness. In order to distinguish relative differences between clusters more easily, anomalies from the frequency-weighted mean across all clusters are provided. Because ship sampling is sparse over southern hemisphere midlatitude oceans, Table 3 includes only northern hemisphere points. This should not bias the results appreciably since no cluster is primarily restricted to the southern hemisphere, and mean cloud properties and dynamics are similar for each cluster in either hemisphere (not shown). There is general agreement but not exact correspondence between Table 1 and Table 3 due to the different spatial scale and method of satellite and surface observations.

Figure 1 displays the mean cloud fraction for all categories in the ISCCP CTP-τ histograms for each of the seven clusters. If mean cloud fraction in a category is less than 2%, it is not displayed. The three most frequent clusters all correspond to low-level cloud regimes, as seen by the predominance of clouds with CTP greater than 680 mb. Since surface observers report small cumulus and clear sky more frequently for Cluster 1 than any other cluster (Table 3), we will refer to it as the "small cumulus" cluster. We call Cluster 2 "large cumulus" and Cluster 3 "stratocumulus/stratus" for similar reasons. Cluster 1 has the smallest cloud fraction of all clusters, and low-level and total cloud fraction increase from Cluster 1 to 2 to 3 (Tables 1 and 3), consistent with their "Small Cu", "Large Cu", and "Sc/St" designations. Clusters 1, 2, and 3 have weak LWCRF (Table 3) because their low cloud tops are relatively warm (Table 1). Cluster 3 has stronger SWCRF than do Clusters 1 and 2, as would be expected for horizontally extensive stratiform cloud.
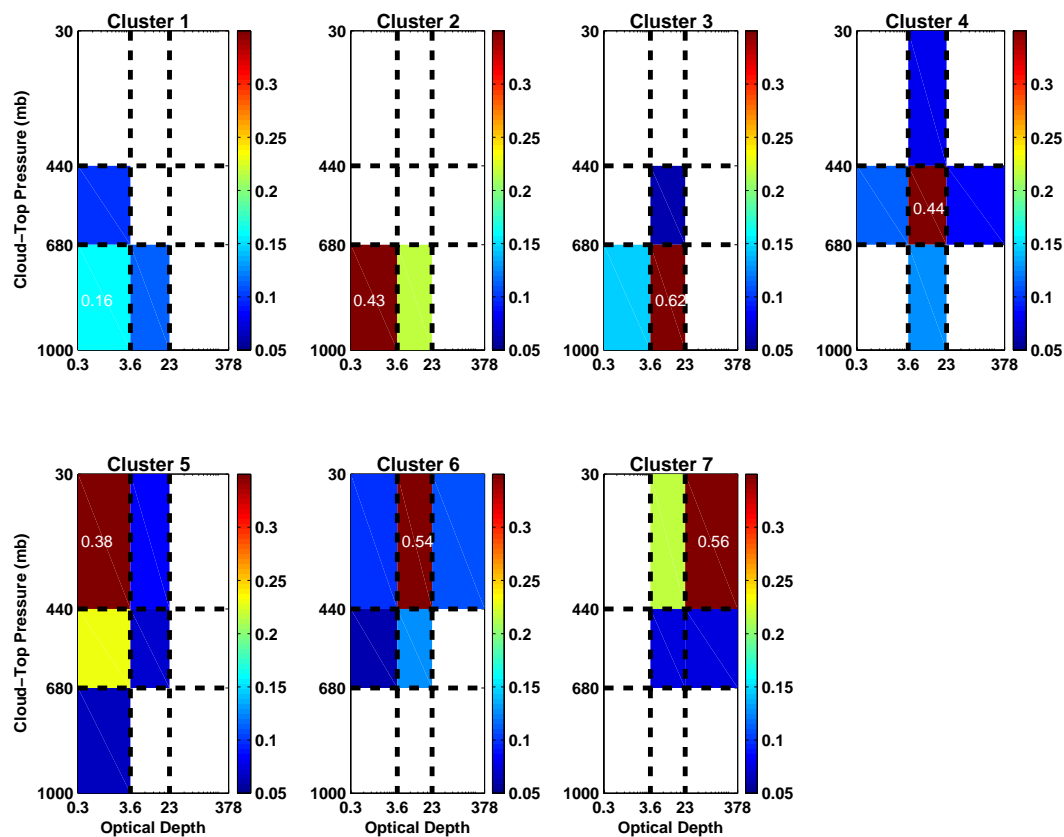
Fig. 1. Mean ISCCP histograms of cloud fraction for each cloud-top pressure and cloud optical thickness interval.

Table 2. Grid box mean ISCCP cloud radiative forcing for each cluster.

	1 – Small Cu	2 – Large Cu	3 – Sc/St	4 – Deep As	5 – Cirrus	6 – Weak Frontal	7 – Strong Frontal
SWCRF (Wm^2)	−39.01	−40.46	−96.96	−112.89	−55.04	−123.05	−168.38
LWCRF (Wm^2)	14.81	10.32	13.17	40.59	46.71	78.26	87.02

Cluster 4 is the only cluster with a cloud top in the middle troposphere (Fig. 1). The large low-level cloud amount and stratiform cloud types very frequently reported by surface observers for this cluster (Table 3) suggest that these clouds usually extend from the middle troposphere down to near the surface, even though the satellite retrievals are unable to provide that information. For this reason, we call Cluster 4 "deep altostratus". Table 2 shows that it has larger LWCRF than the low-level cloud clusters and relatively strong SWCRF.

The last three clusters in Fig. 1 are high-top cloud regimes with optical thickness that increases from Cluster 5 to 6 to 7. We call Cluster 5 "cirrus" because it has the smallest optical thickness and least low-level cloud of all clusters (Tables 1 and 3). The magnitude of SWCRF is only slightly larger than

the magnitude of LWCRF for Cluster 5 (Table 2), which is the only case where the cooling from reflected solar radiation is nearly cancelled out by the trapping of longwave radiation emitted by the surface. Clusters 6 and 7 contrastingly have a large cooling effect on climate because their very negative SWCRF substantially outweighs their large positive LWCRF. As was the case for Cluster 4, surface observers report large low-level cloud amount by stratiform types, indicating that Clusters 6 and 7 have vertically extensive clouds. Surface observers also report the occurrence of precipitation 13% of the time for Cluster 6 and 30% of the time for Cluster 7 (Table 3). We call Cluster 6 "weak frontal" and Cluster 7 "strong frontal." The net CRF values (i.e., SWCRF+LWCRF) for the "weak frontal" and "strong frontal" regimes are −45 and −81 Wm^2, respectively, consistent with the approximate

Table 3. Mean surface-reported cloud properties for each cluster (northern hemisphere only), along with anomaly from the average over all clusters.

Observation		Cluster #						
		1	2	3	4	5	6	7
Clear-sky Frequency (%)	Mean	6.8	2.2	1.1	0.4	3.5	0.4	0.2
	Anom	3.7	−0.9	−2.0	−2.6	0.4	−2.7	−2.9
Obscured-sky Frequency (%)	Mean	2.2	2.1	10.5	9.3	1.8	9.1	12.5
	Anom	−3.3	−3.4	5.0	3.8	−3.8	3.6	6.9
Total Cloud Amount (%-sky-cover)	Mean	58.2	68.5	87.1	90.7	67.4	92.6	95.9
	Anom	−16.5	−6.3	12.4	15.9	−7.4	17.9	21.1
Low-level Cloud Amount (%-sky-cover)	Mean	47.2	59.7	79.9	80.9	48.7	79.9	86.4
	Anom	−16.6	−4.1	16.1	17.1	−15.1	16.1	22.6
Rain and Snow Frequency (%)	Mean	4.2	6.4	4.6	11.5	3.0	13.1	30.1
	Anom	−3.3	−1.1	−2.9	4.0	−4.5	5.6	22.6
No-low-cloud Frequency (%)	Mean	16.3	6.4	4.9	4.7	17.8	5.6	3.9
	Anom	6.2	−3.7	−5.3	−5.4	7.7	−4.5	−6.2
Small Cumulus Frequency (%)	Mean	18.5	13.7	5.1	4.5	15.7	4.7	2.5
	Anom	7.1	2.3	−6.3	−6.9	4.4	−6.7	−8.8
Moderate and Large Cumulus Frequency (%)	Mean	16.8	18.6	6.9	6.5	14.1	5.8	3.8
	Anom	4.7	6.5	−5.3	−5.7	1.9	−6.4	−8.3
Mixed Cumulus and Stratocumulus Frequency (%)	Mean	16.9	22.5	20.2	19.3	18.8	18.1	12.3
	Anom	−1.8	3.7	1.5	0.6	0.1	−0.6	−6.4
Ordinary Stratocumulus Frequency (%)	Mean	9.6	18.6	20.6	18.3	12.1	16.7	13.7
	Anom	−4.4	6.5	6.6	4.4	−1.8	2.8	−0.3
Fair-weather Stratus Frequency (%)	Mean	5.5	5.8	15.4	15.7	6.3	16.2	17.9
	Anom	−4.6	−4.3	5.2	5.6	−3.9	6.1	7.8
Bad-weather Stratus Frequency (%)	Mean	6.1	7.5	11.4	16.0	6.2	18.5	28.0
	Anom	−4.5	−3.2	0.8	5.4	−4.4	7.9	17.3

$-70 \, \text{Wm}^2$ value reported by Weaver and Ramanathan (1996) for midlatitude ocean synoptic storms. Averaging over all clusters with weighting by their relative frequencies, we calculate a net CRF cooling of $-39 \, \text{Wm}^2$ by midlatitude ocean clouds.

As mentioned previously, our clustering algorithm may converge to a different solution, depending on the initial seeds provided. We resolved this by taking the solution with the smallest total variance. Besides the solution presented in Fig. 1, there are two additional sets of clusters to which the solution can converge. The only difference is the inclusion of either another low-level cloud or midlevel cloud cluster, both of which occur with the loss of one of the frontal clusters. In analyzing clustering results for values of k greater than seven, we often found cases with more than three low-level cloud clusters or more than one midlevel cloud cluster. In both of these instances, the inclusion of the additional cluster did not provide any additional information since the cluster with intermediate cloud properties also exhibited intermediate meteorological properties. Clustering analysis independently applied to individual ocean basins and seasons produced types similar to those described above, albeit with possibly different frequencies.

5 Characteristic dynamics

To provide insight into the atmospheric state and advective forcing associated with the various cloud regimes, we averaged vertical profiles of NCEP/NCAR Reanalysis data over the grid boxes and times corresponding to each cluster. Monthly means for each spatial point and each vertical level were removed from all meteorological parameters to prevent spatial and seasonal biases from affecting the results. Thus, meteorological conditions associated with the clusters will represent perturbations from the mean state. The advective tendencies of water-vapor mixing ratio were converted to tendencies in relative humidity (RH) by dividing by the saturation-mixing ratio at each level. For consistency, we chose all values of RH and saturation with respect to liquid water even though saturation with respect to ice may be more applicable in the upper troposphere. Additionally, the meridional wind for all points in the southern hemisphere was multiplied by -1 before averaging so that positive horizontal flow is in a poleward sense. Vertical profiles of perturbation RH are displayed in Fig. 2, perturbation temperature in Fig. 3, perturbation pressure vertical velocity in Fig. 4, perturbation horizontal advective tendencies of water-vapor mixing ratio in Fig. 5, and perturbation horizontal advective tendencies
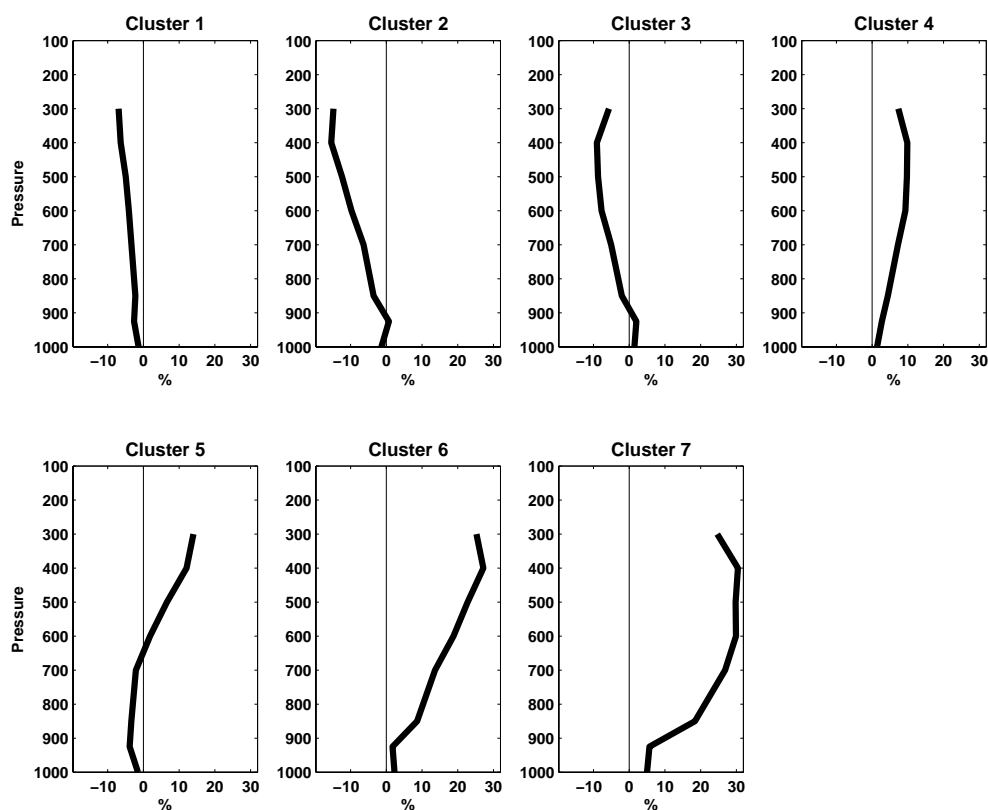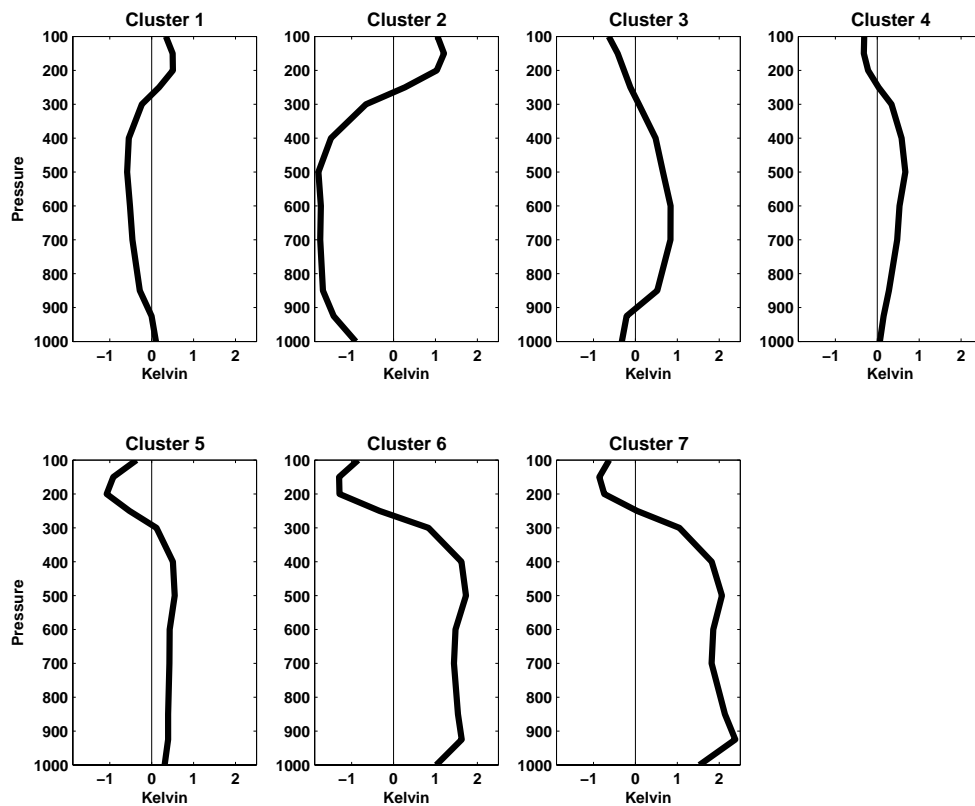
Fig. 2. Vertical profiles of mean perturbation relative humidity for each cluster from the NCEP Reanalysis.

of temperature in Fig. 6. Profiles of vertical advection tendencies of both temperature and water vapor (not shown) are similar to the profile of vertical motion (water vapor being the opposite sign). We have not included bars corresponding to the 95% confidence interval on either side of the profiles because, in nearly every instance, the uncertainty range was indistinguishable from the mean profile (due to the very large number of data points contributing to each cluster).

The mean cloud properties of each cluster are physically consistent with the meteorological state and dynamical forcing. The low-level cloud Clusters (1, 2, and 3) occur with negative perturbation RH in the middle and upper troposphere (Fig. 2) that is produced by grid box mean vertical descent (Fig. 4). Cluster 1 (Small Cu) has the weakest average dynamical forcing, with near-mean profiles in temperature (Fig. 3), zonal and meridional wind (not shown), horizontal advection of moisture (Fig. 5), and horizontal advection of temperature (Fig. 6). Clusters 2 and 3 have similar dynamics (downward motion and low-level horizontal advective perturbation drying and cooling), but their temperature profiles are quite different. Cluster 2 (Large Cu) occurs with a relatively cold boundary layer and cold free troposphere, whereas Cluster 3 (Sc/St) occurs with a relatively cool boundary layer and relatively warm free troposphere (thus indicating a perturbation temperature inversion). These characteristics are con-

sistent with the vertical temperature profile and dynamical processes previously found to be associated with surface-observed midlatitude large cumulus and stratocumulus, respectively (Norris, 1998a; Norris and Klein, 2000). In the Large Cu cluster, perturbation temperature switches from cold below 300 mb to warm above 300 mb, suggesting a depressed tropopause. Contrastingly, the Sc/St cluster has an opposite temperature reversal – warm below and cold above 300 mb, suggesting a slightly elevated tropopause (Fig. 3).

Clusters 6 (Weak Frontal) and 7 (Strong Frontal) appear to occur east of the trough and west of the ridge in a midtropospheric synoptic wave. Both occur with strong upward motion (Fig. 4) and a very moist troposphere (Fig. 2). Although not shown, perturbation horizontal velocity in the upper troposphere is southwesterly (in a northern hemisphere sense), which is consistent with the positive perturbation temperature advection (Fig. 6), warm tropospheric temperature, and elevated tropopause (Fig. 3). Figure 5 indicates that both frontal clusters have horizontal perturbation moistening in the lower troposphere, and the strong upward moisture advection clearly dominates the horizontal perturbation drying in the upper troposphere to create vertically extensive cloudiness. Consistent with the names of the clusters, the Weak Frontal cluster has smaller perturbations in meteorological state and dynamical forcing than the Strong Frontal cluster.

Fig. 3. As in Fig. 2, except for perturbation temperature.

Cluster 4 (Deep As) exhibits vertical profiles of perturbation RH, temperature, vertical velocity, horizontal temperature advection, and horizontal moisture advection that have similar shapes and signs, albeit with much weaker magnitude, to those of the frontal clusters.

The RH profile for Cluster 5 (Cirrus) shows negative perturbation moisture below 600 mb and significant positive perturbation moisture above 600 mb (Fig. 2), and the negative temperature perturbation above 250 mb (Fig. 3) suggests that it coincides with an elevated tropopause. The large positive horizontal perturbation moisture advection (Fig. 5) suggests that some of these clouds are blow-off from a deep convective system or an extratropical cyclone, and the small upward motion in the upper troposphere suggests that some of these clouds may be locally dynamically generated (Fig. 4).

In addition to looking at the local meteorological conditions, we can examine the spatial relationships between cloud regimes corresponding to each cluster. This can be accomplished by compositing the frequency of occurrence of various clusters in grid boxes surrounding a central point (e.g., Lau and Crane, 1995; Norris and Iacobellis, 2005). In this case we choose as a central point those grid boxes in which the Strong Frontal cluster is present. To avoid biases from geographical and seasonal variations in cluster distribution, we subtracted the long-term monthly mean cluster

frequency for each grid box before adding it to the composite. Figure 7 shows the results, which are generally consistent with the placement of cloud regimes in a midlatitude synoptic wave. Points located in the Southern Hemisphere have been inverted before averaging so that the figure is displayed in a Northern Hemisphere sense, namely the bottom of the domain is towards the equator. By construction, there is a large positive perturbation in the frequency of Cluster 7 (Strong Frontal) at the center of the composite. Similar to Lau and Crane (1995), who composited on points of high optical thickness, Cluster 7 frequency is preferentially oriented in a SW-NE fashion (in a northern hemisphere sense). Cluster 6 (Weak Frontal) is also relatively frequent in the region surrounding the center, especially to the northeast (in a northern hemisphere sense). The frequency of Cluster 5 (Cirrus) is enhanced equatorward and eastward (i.e., ahead) of the frontal regime. Clusters 1 (Small Cu) and 2 (Large Cu) more frequently occur northwest of the frontal regime (i.e., in the cold sector).

6 Spatial distribution and seasonal cycle

Figure 8a–g show the spatial distribution of the annual mean frequency of each cluster. Note that some artificial features associated with the viewing geometry of geostationary
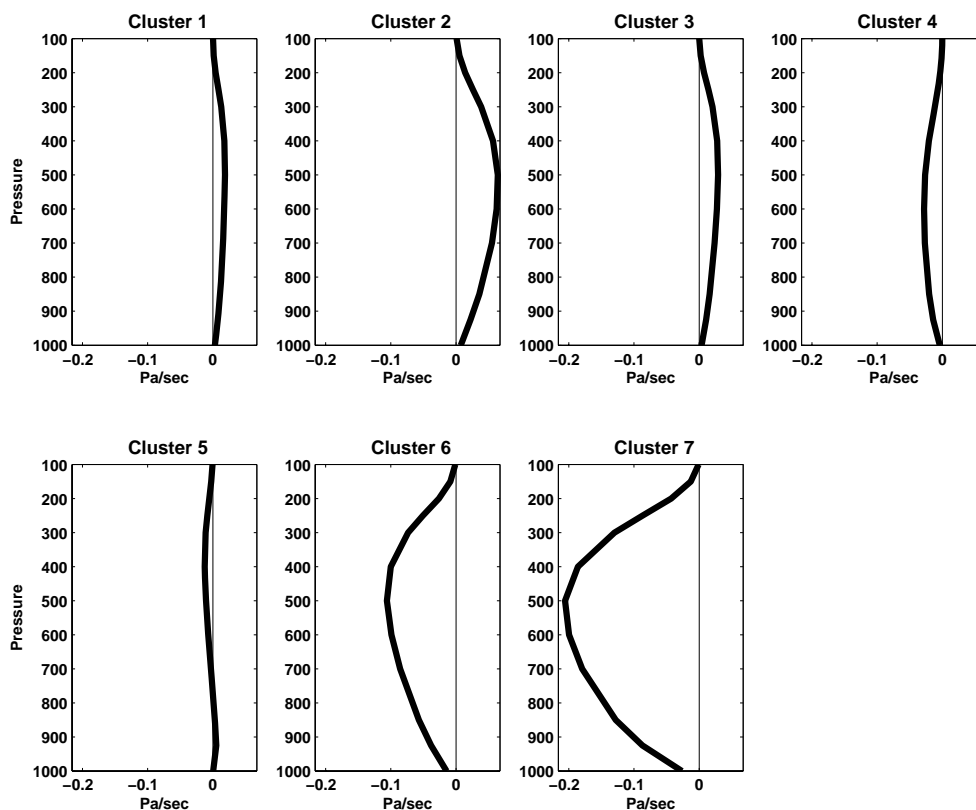
Fig. 4. As in Fig. 2, except for perturbation pressure vertical velocity.

satellites are present and do not reflect real geographical variations (Rossow and Garder, 1993). The overall most frequent cluster, Small Cu, predominantly occurs in equatorward and coastal regions of our domain (Fig. 8a), as may be expected for the cluster with the least cloud fraction and greatest prevalence of surface-reported cumuliform cloud types (Table 3 of this study; Figs. 5 and 6 of Norris, 1998b). The CTP-τ histogram for Small Cu (Fig. 1) shows that this cluster is primarily composed of low-level clouds, but some small amount of higher clouds is mixed in, as implied by the lower grid box mean CTP for this cluster relative to the other low-level cloud clusters (Table 1). The second cluster, Large Cu, occurs more often in the center of the ocean basins and is more prevalent in the southern hemisphere (Fig. 8b). The final low-level cloud cluster, Sc/St, has a very distinctive geographical distribution. The region of highest frequency is the subtropical anticyclone region in the eastern Pacific Ocean, and other regions of frequent Sc/St include the far northern Pacific Ocean and off the west coast of Australia (Fig. 8c). Other climatological subtropical stratocumulus regions are too far equatorward to be included in our analysis (Norris, 1998b).

The only predominantly midlevel cluster, Deep As, is primarily located in the higher latitude regions of the analysis domain (Fig. 8d). Cluster 5 (Cirrus) is most frequent immediately east of continents (South America, North Amer-

ica, and southern Africa). Another region of increased frequency is in the central Pacific, possibly due to advection from the deep convective towers of the west Pacific equatorial warm pool (Fig. 8e). The final two clusters (Weak Frontal and Strong Frontal) are fixtures of the storm track, with the Strong Frontal cluster more focused in the western half of the ocean basins (Fig. 8f–g).

Williams and Tselioudis (2007) (hereafter WT07) performed a similar study by clustering ISCCP histograms for the ice-free extratropics (poleward of 20° in both hemispheres). Although they only examine five cloud clusters, their results are very similar to those produced from our analysis (Fig. 6 from WT07). The WT07 clusters of shallow cumulus, stratocumulus, cirrus, mid-level, and frontal are similar to Small Cu, Sc/St, Cirrus, Deep As, and Strong Frontal (respectively). The WT07 study examined a much larger domain, allowing points poleward of 55°, provided that they are ice-free, more subtropical points, and points over land.

In order to gain a more in-depth understanding of the relationship of each cluster to large-scale dynamical processes, it is useful to examine the seasonal cycle of each cluster's spatial distribution. For Cluster 1 (Small Cu), the spatial distribution of each season is nearly identical to that of the annual mean and is therefore not shown. Figure 9a and b display the spatial distribution of Cluster 2 (Large Cu) for the December-January-February (DJF) and June-July-
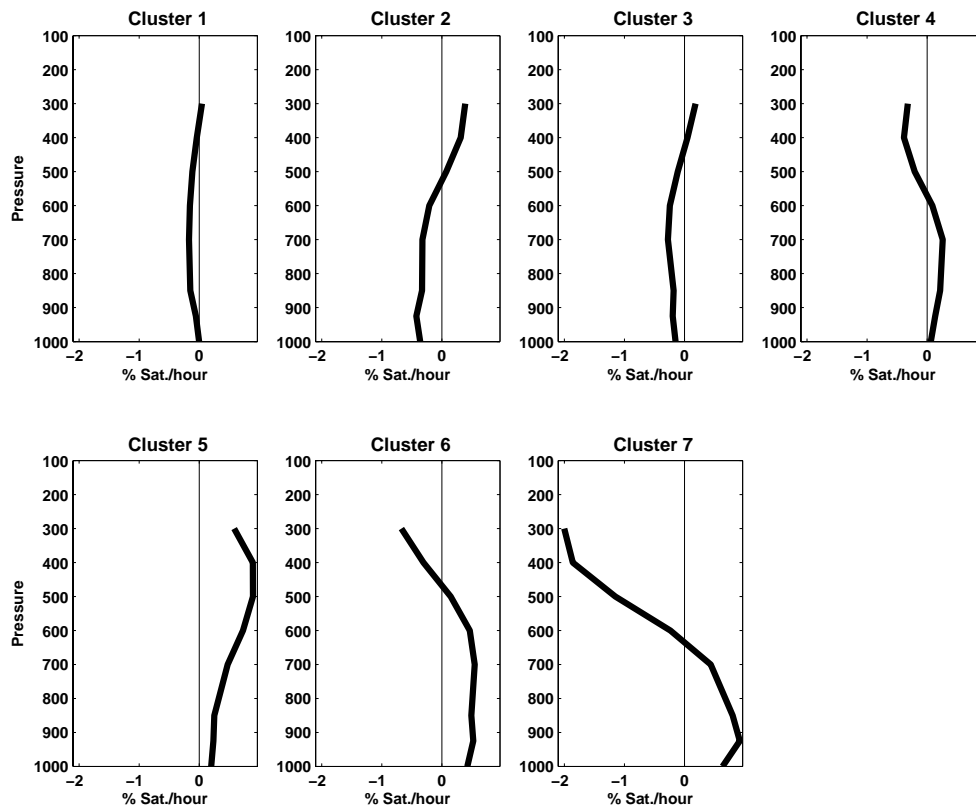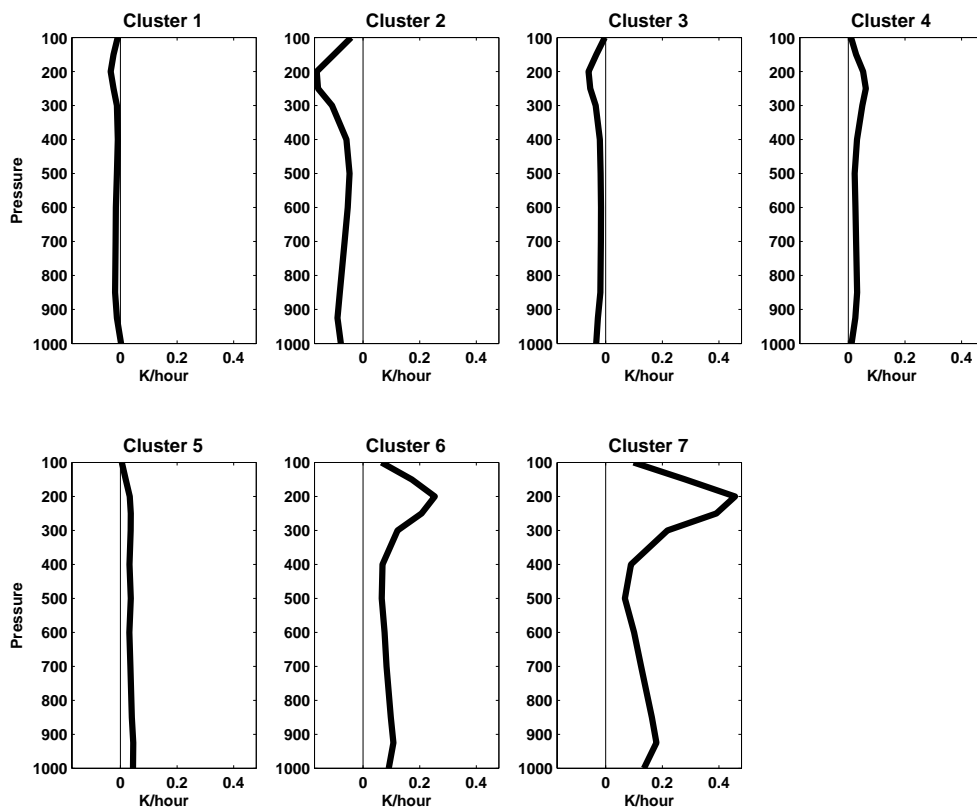
Fig. 5. As in Fig. 2, except for perturbation horizontal moisture advection.

August (JJA) seasons, respectively. This cloud regime predominantly occurs in the winter season, suggesting that these clouds are the result of cold air advecting over warmer water behind a frontal system (Fig. 7). Cluster 3 (Sc/St) also has a very strong seasonal cycle (Fig. 10a–b), but unlike Cluster 2, it primarily occurs during the summer season. Stratocumulus clouds in the eastern Pacific anticyclone region and stratus clouds in the central North Pacific are most extensive during JJA (Norris, 1998b).

The spatial distribution of Cluster 4 (Deep As) frequency for each season is fairly similar to the mean distribution (not shown). One large exception is the North Pacific during JJA, where Deep As is especially prevalent (Fig. 11). The restriction of this cloud regime to higher latitudes and its increased frequency in northern hemisphere summer suggests that these are weakly forced and shallow synoptic storms. Surface observers report precipitation for the Deep As cluster nearly as often as they do for the Weak Frontal cluster (Table 3). Cluster 5 (Cirrus) also has little seasonality for the most part. One exception is that the frequency of Cirrus is enhanced in the western North Pacific Ocean near the southern boundary of our domain during JJA (Fig. 12). These high-level clouds may be the result of greater nearby convection in the western tropical warm pool.

7 Temperature sensitivty analysis method

Since previous studies (e.g., Bony et al., 2004) have suggested the thermodynamic component of cloud change will be globally more influential than the dynamical component of cloud change, we would like to understand the impact that increasing temperature has on cloud properties. To this end, we divided clusters into relatively warm and relatively cold sub-groups according to tropospheric mean temperature. We use tropospheric temperature rather than SST to act as a proxy for anthropogenic global warming because tropospheric temperature has much more variance at daily time scales than SST and best represents the temperature experienced by clouds. Tropospheric mean temperature is the pressure-weighted average of temperature at levels from 1000 mb to 200 mb. In order for a case to be considered relatively warm (or cold), it had to be above (or below) the median of tropospheric mean temperature for each ISCCP grid box, calendar month, and cluster number. This uniform sampling ensures that no geographical or seasonal biases are introduced. As observed by Norris and Iacobellis (2005), temperature advection is a large contributor to local temperature variability. In order to eliminate a possible confounding dynamical influence, we require that all cases be between the 25th and 75th percentile of horizontal

Fig. 6. As in Fig. 2, except for perturbation horizontal temperature advection.

and vertical temperature advection. This is conducted independently for three different layers of the atmosphere, which corresponded to the layers of the ISCCP cloud histograms (1000–680 mb, 680–440 mb, and 440–100 mb). Examining warm-cold differences in cloud properties only for conditions of median advection minimizes the possibility of misinterpreting a cloud-temperature relationship produced by large-scale dynamics for a thermodynamic response. Such confusion could arise because variability in cloud amount, temperature, advection, and the storm track are closely connected over midlatitude oceans (Norris, 2000).

Two more meteorological conditions that we restricted were lower-tropospheric static stability (LTS) and the tropopause height. The former has particular influence on low-level cloud properties (Klein and Hartmann, 1993; Norris, 1998), while the latter primarily affects the high-cloud clusters. Because advection over the ocean produces a greater change in temperature in the mid-troposphere than near the surface, warm cases are on average associated with stronger stability than cold cases. To minimize the confounding influence of changes in LTS on cloud-temperature relationships, we required that the temperature difference between 1000 mb and 70 mb be between the 25th and 75th percentiles. For the high-cloud clusters, warm cases tend to occur with a higher tropopause, which allows clouds to extend

to greater elevation. To minimize this effect, we required that the temperature difference between 200 mb and 400 mb be between the 25th and 75th percentiles (thus constraining variations in tropopause height). These restrictions were applied independently to each ISCCP grid box, calendar month, and cluster number with an equal number of warm and cold cases retained. Although midlatitude lapse rate will probably decrease with global warming, albeit much less so than in the tropics (Fig. 10.7 of IPCC, 2007), we did not attempt to reproduce this in differences between warm and cold cases because that would have required complicated additional composite restrictions,

Our division of the initial 10 million daily grid box observations into warm and cold subsets for conditions of median advection and lapse rate in three layers of the troposphere left us with about 75 000 observations designated as warm and an equal number as cold. Since the warm and cold observations were uniformly distributed geographically and seasonally in proportion to cluster frequency, our results are globally representative of clouds over midlatitude oceans. Assuming that observations are independent if they are not in adjacent grid boxes and separated by more than one day in time, the effective number of observations, N_{eff}, is about 1/4 of the nominal number of observations, N.
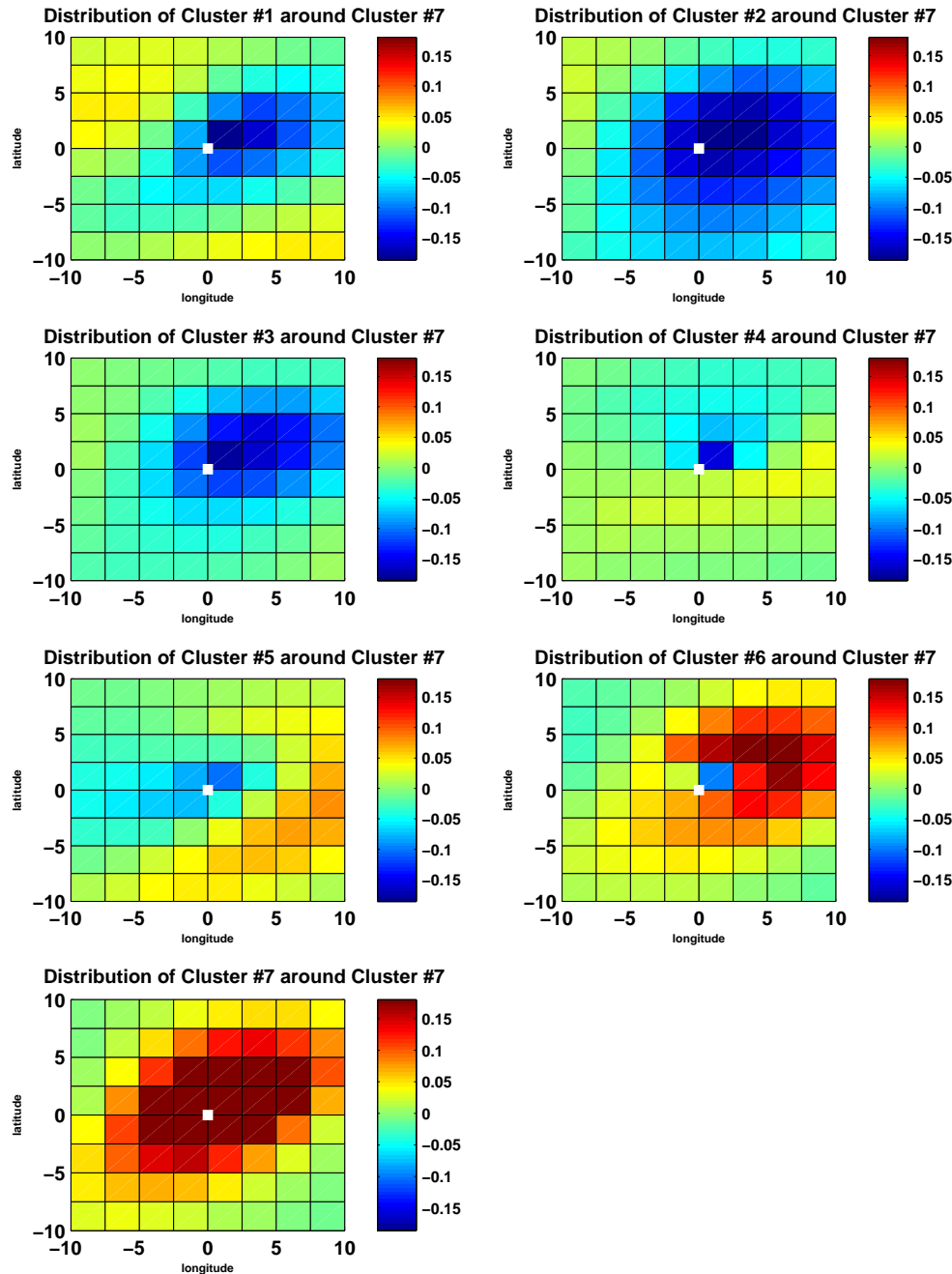
Fig. 7. Composite spatial distributions of the perturbation frequency of each cluster around a central grid box with the Strong Frontal cluster.

8 Impact of increasing temperature on cloud properties

Since we are interested in how cloud properties change with increasing tropospheric temperature, we examined differences between the warm and cold cases. Figure 13 shows IS-CCP CTP-τ histograms for the average warm minus cold difference in cloud fraction for each of the seven clusters. Unshaded areas of the histograms represent regions where the difference was not significant at the 95% confidence level.

We calculated confidence levels using a bootstrap method wherein two sets of N_{eff} values were randomly selected from the combined set of N warm $+N$ cold observations for each cluster, and the average difference between the two sets was calculated. This procedure was repeated 1000 times to determine how likely the observed difference could have occurred by chance. Table 4 shows cluster average, warm average, cold average, and warm-cold differences in grid box mean cloud properties for each cluster per degree change in
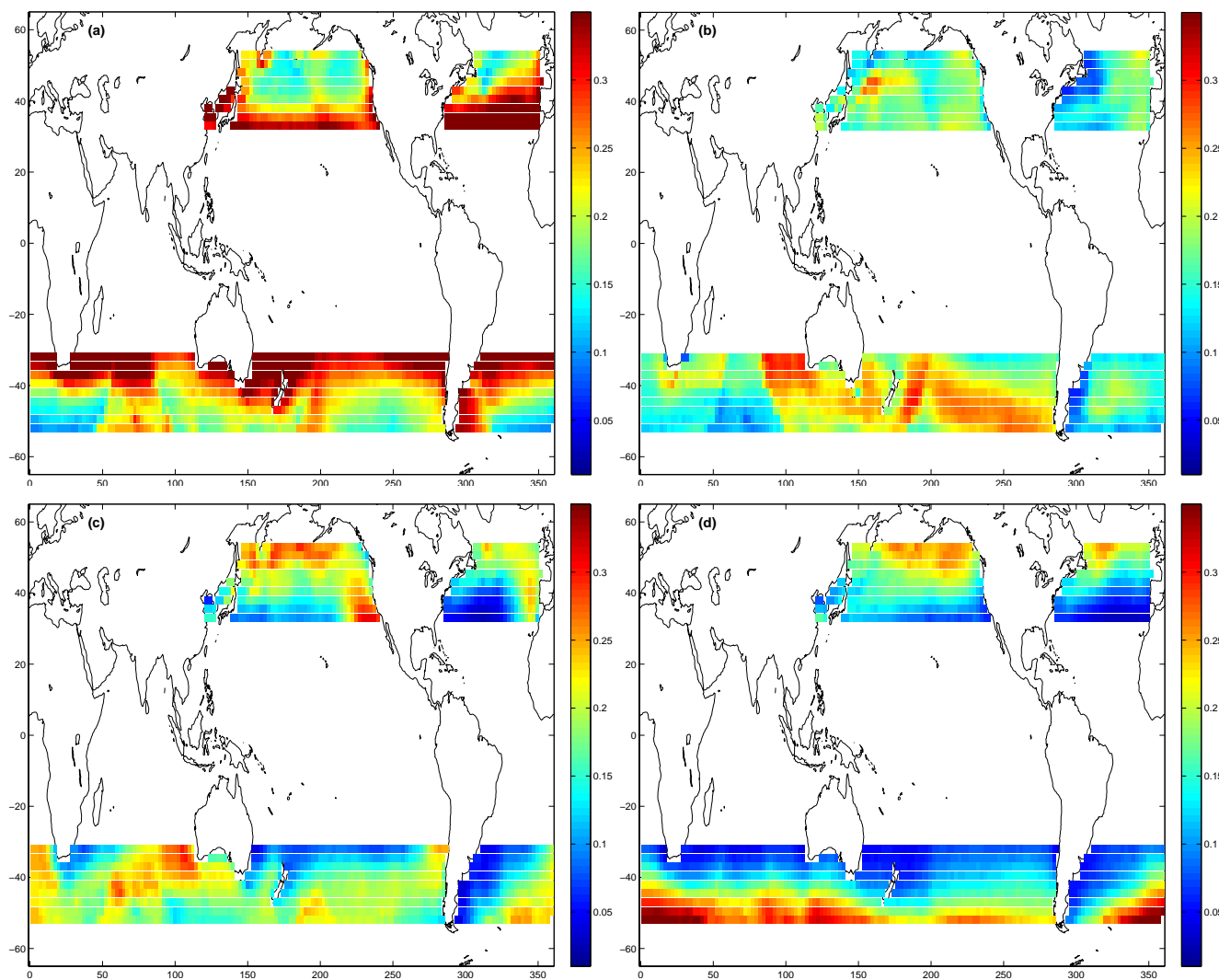
Fig. 8. Annual mean climatological spatial distributions of the frequency of each cluster, **(a)** Small Cumulus, **(b)** Large Cumulus, **(c)** Stratocumulus/Stratus, **(d)** Deep Altostratus, **(e)** Cirrus, **(f)** Weak Frontal, and **(g)** Strong Frontal.

temperature. Those differences that are different from zero at the 95% confidence level are displayed in bold in Table 4. We used an ISCCP look-up table (corresponding to Fig. 3.13 in Rossow et al., 1996) to convert visible cloud optical thickness to infrared window cloud emissivity.

Figure 13 and Table 4 show a generally consistent reduction in cloud fraction, increase in cloud-top pressure (lowering of cloud top), and increase in optical thickness across all clusters for increasing temperature. Cluster 1 (Small Cu) exhibits the largest decrease in cloud fraction at -2.3% K^{-1}, accompanied by increases in cloud-top pressure and optical thickness. The other low-level cloud clusters (Large Cu and Sc/St) have smaller reductions in cloud fraction and larger increases in cloud-top pressure ($+6.9$ and $+9.1$ mb K^{-1}, respectively). The enhancement of optical thickness for the small Cu and Large Cu clusters ($+0.13$ K^{-1} and $+0.09$ K^{-1}, respectively) is produced by a decrease in the occurrence of

optically thin clouds and an increase in the occurrence of optically thick clouds within the grid box (Fig. 13). Cluster 3 (Sc/St) is the only cluster with a reduction in optical thickness for increasing temperature (-0.05 K^{-1}), which is due to a decrease in the occurrence of optically thick clouds (Fig. 13).

Cluster 4 (Deep As) shows little change in cloud fraction or cloud-top pressure but has the largest change in optical thickness ($+0.33$ K^{-1}), as seen in Table 4. The latter is produced by a decrease in the occurrence of optically thin clouds and an increase in the occurrence of optically thick clouds (Fig. 13). Cluster 5 (Cirrus) exhibits a reduction in cloud fraction (-0.9% K^{-1}), and it is the only cluster with a substantial decrease in cloud-top pressure (-3.8 mb K^{-1}) caused by a reduction in the occurrence of low-level clouds. For the weak frontal cluster, the only significant change with warmer temperature is an increase in optical thickness of
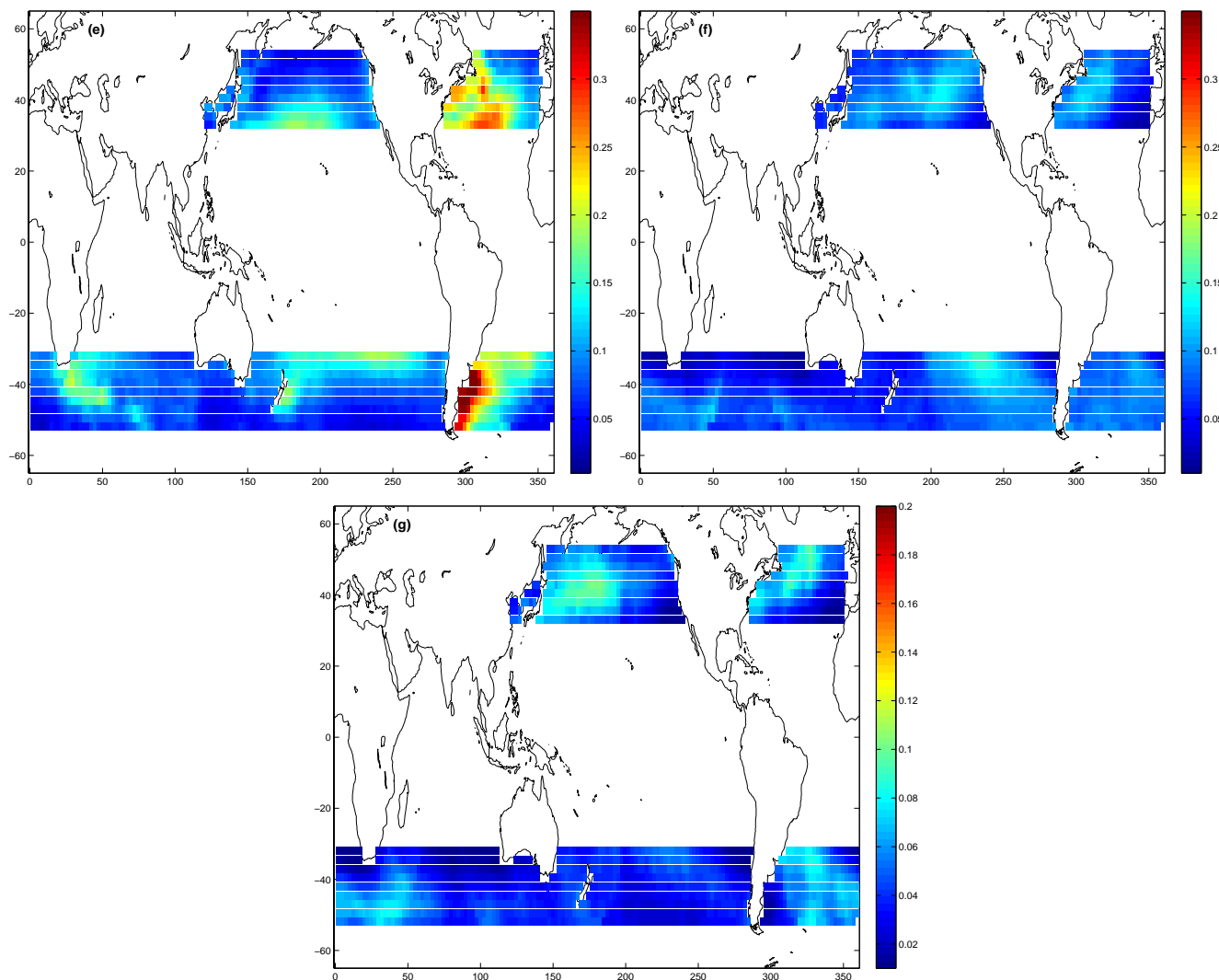
Fig. 8. Continued.

+0.25 K^{-1} due to the more frequent occurrence of optically thick clouds. The strong frontal cluster exhibits no significant changes with increasing temperature (Table 4).

Although there is substantial noise due to small sample sizes for individual grid boxes, the geographical and seasonal distributions of differences in cloud properties between warm and cold subsets for a given cluster appear to be uniform (not shown). This suggests that the information in Table 4 represents the general response of various cloud regimes to warming rather than a particular response driven by a change only in one region or season.

To provide context for how cloud properties change with temperature, we present the average vertical profiles of meteorological parameters derived from NCEP Reanalysis for the warm and cold subsets of each cluster. Figure 14 shows the vertical profiles of temperature anomalies with respect to grid box and calendar month means. By construction,

the warm subset has warmer tropospheric temperature than the cold subset, with the average cluster temperature profile (Fig. 3) lying between them. Although the anomalies are not vertically uniform, the difference between warm and cold profiles is nearly constant within the troposphere, suggesting that the cloud differences cannot be ascribed to differences in lapse rate. Figure 15 shows relative humidity anomalies for warm and cold subsets, and warm cases have a greater grid box relative humidity that is statistically significant and extends over a larger vertical range than cold cases. The implied increase in geometric thickness for warm-subset clouds is consistent with the tendency for larger cloud optical thickness but not with the tendency for greater cloud-top pressure (Table 4). Specific humidity anomalies are substantially larger in the lower troposphere for the warm subset (Fig. 16), as may be expected from the increase in saturation-specific humidity with increasing temperature. Vertical velocity has
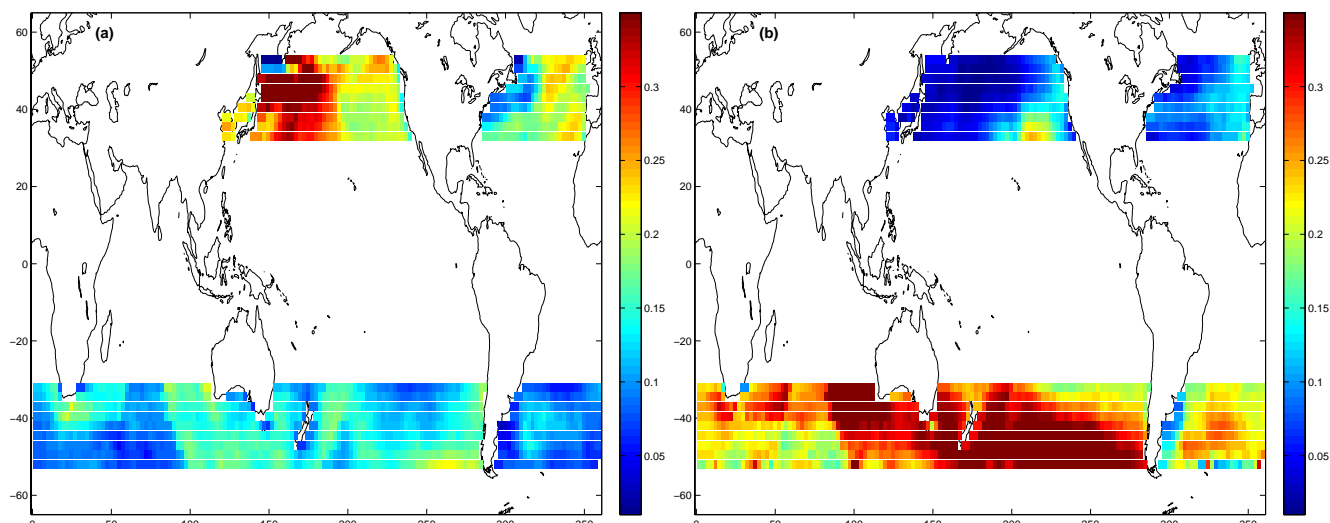
Fig. 9. Seasonal mean climatological spatial distributions of the frequency of Cluster 2 (Large Cumulus), **(a)** DJF and **(b)** JJA.
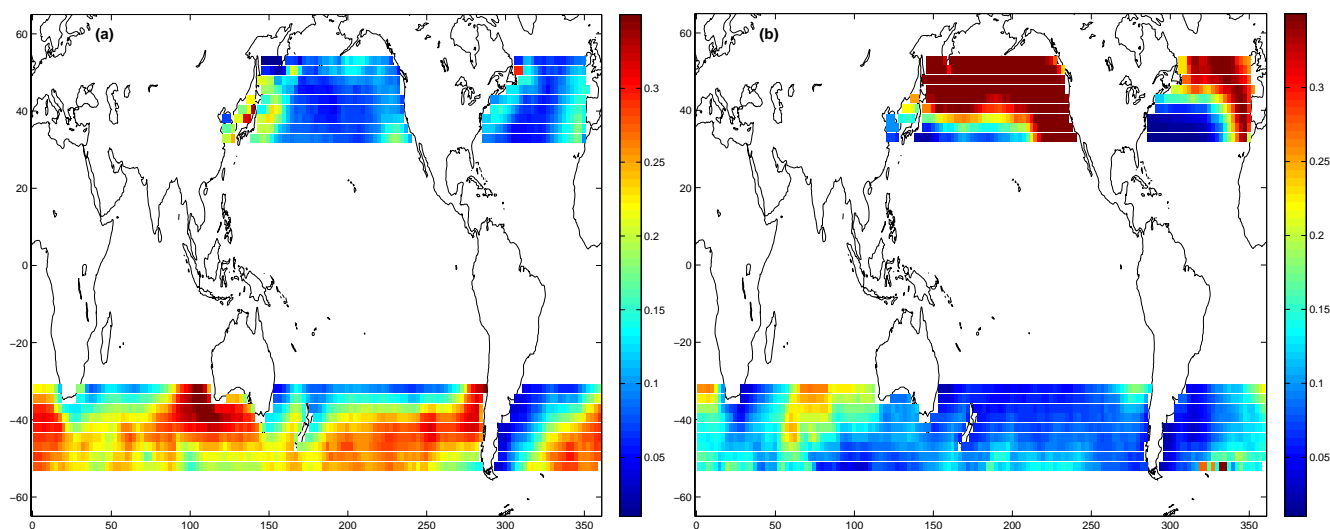
Fig. 10. As in Fig. 9, except for Cluster 3 (Stratocumulus/Stratus), **(a)** DJF and **(b)** JJA.

a large influence over midlatitude ocean cloudiness (Lau and Crane, 1995; Norris and Klein, 2000; Weaver and Ramanathan, 1997), and Fig. 17 shows that vertical profiles of vertical velocity anomalies are almost exactly the same for warm and cold subsets. This result gives us confidence that our restriction of temperature advection to near-median values successfully eliminated differences in the large-scale dynamical forcing of clouds in the warm and cold subsets of each cluster.

9 Impact of increasing temperature on radiative properties

The effects of temperature modification of cloud properties on the climate system can be better understood by examining changes in radiation flux. Table 5 shows the TOA SW cloud radiative forcing (SWCRF) averaged over the entire cluster, only warm cases, only cold cases, and their difference. Following Ramanathan et al. (1989), we define SWCRF as clear-sky upwelling flux minus all-sky upwelling flux; thus negative values have a cooling effect on climate. Note that all-sky flux includes flux from both clear and cloudy portions of a grid box. In order to understand how changes in cloud fraction and optical thickness separately affect SWCRF, we divide it into the following components,

Table 4. Average cloud properties for the entire cluster, warm subset, cold subset, and the difference between the two divided by the temperature change for each cluster (Subsets different at the 95% confidence level are in bold).

	1 – Small Cu	2 – Large Cu	3 – Sc/St	4 – Deep As	5 – Ci	6 – Weak Frontal	7 – Strong Frontal
Cluster Frequency (%)	27.5	18.4	16.5	14.0	11.3	7.7	4.3
Warm – Cold Difference (K)	2.25	2.23	2.25	2.58	2.37	2.45	2.37
Cluster Cloud Fraction (%)	54.1	77.8	92.9	97.5	87.4	99.0	99.4
Warm Subset (%)	45.5	75.8	92.0	97.7	85.0	99.3	99.5
Cold Subset (%)	50.7	77.1	92.9	97.9	87.0	99.4	99.5
Difference (% K^{-1})	**−2.3**	**−0.6**	**−0.4**	−0.1	**−0.9**	0.0	0.0
Cluster CTP (mb)	658.2	781.0	776.4	584.3	431.8	382.6	347.6
Warm Subset (mb)	679.2	799.2	795.0	588.1	425.2	389.1	350.9
Cold Subset (mb)	668.7	783.8	774.5	589.5	434.1	388.5	349.0
Difference (mb K^{-1})	**+4.6**	**+6.9**	**+9.1**	−0.5	**−3.8**	+0.3	+0.8
Cluster Optical Thickness	3.63	2.89	7.19	8.30	2.30	8.90	23.08
Warm Subset	3.32	2.89	7.07	8.30	2.12	9.06	22.63
Cold Subset	3.03	2.69	7.19	7.46	2.06	8.44	22.63
Difference (K^{-1})	**+0.13**	**+0.09**	−0.05	**+0.33**	+0.03	**+0.25**	0.00
Cluster Emissivity	0.835	0.823	0.979	0.985	0.776	0.993	1.000
Warm Subset	0.825	0.823	0.979	0.986	0.750	0.994	1.000
Cold Subset	0.802	0.805	0.978	0.981	0.746	0.992	1.000
Difference (K^{-1})	**+0.010**	**+0.008**	0.000	**+0.002**	+0.002	+0.001	0.000

Table 5. Average total SWCRF, SWCRF from cloud fraction change, and SWCRF from albedo change for entire the cluster, warm subset, cold subset, and the difference between the two (per degree temperature change; Subsets different at the 95% confidence level are in bold).

	1 – Small Cu	2 – Large Cu	3 – Sc/St	4 – Deep As	5 – Ci	6 – Weak Frontal	7 – Strong Frontal
Cluster Total SWCRF (Wm^{-2})	−39.0	−40.5	−97.0	−112.9	−55.0	−123.1	−168.4
Warm Subset (Wm^{-2})	−30.8	−38.8	−93.9	−113.1	−51.1	−125.2	−167.1
Cold Subset (Wm^{-2})	−32.3	−38.5	−96.6	−109.3	−51.8	−122.6	−167.2
Difference (Wm^{-2} K^{-1})	**+0.7**	−0.2	**+1.2**	**−1.5**	+0.3	−1.1	+0.1
SWCRF$_{CF}$							
Warm Subset (Wm^{-2})	−25.7	−36.7	−95.3	−111.13	−47.3	−117.3	−162.8
Cold Subset (Wm^{-2})	−28.6	−37.3	−96.3	−111.35	−48.5	−117.4	−162.8
Difference (Wm^{-2})	**+1.3**	+0.3	+0.5	+0.1	+0.5	+0.1	0.0
SWCRF$_{albedo}$							
Warm Subset (Wm^{-2})	−27.5	−37.4	−95.0	−113.2	−48.0	−118.7	−162.7
Cold Subset (Wm^{-2})	−26.8	−36.5	−96.6	−109.3	−47.9	−116.1	−162.8
Difference (Wm^{-2})	−0.3	−0.4	+0.7	**−1.5**	0.0	−1.1	+0.1

$$SWCRF = -f\alpha SW\downarrow^{TOA} \tag{1}$$

$$\alpha = \alpha_{overcast} - \alpha_{clear} = \frac{SW\uparrow_{overcast}^{TOA} - SW\uparrow_{clear}^{TOA}}{SW\downarrow^{TOA}} \tag{2}$$

where f is cloud fraction and α is the difference between the albedo of an overcast scene and the clear-sky albedo. Albedo values were obtained by dividing TOA upwelling SW flux by insolation. For all clusters, the changes to clear-sky albedo are smaller than the changes to the albedo of the overcast
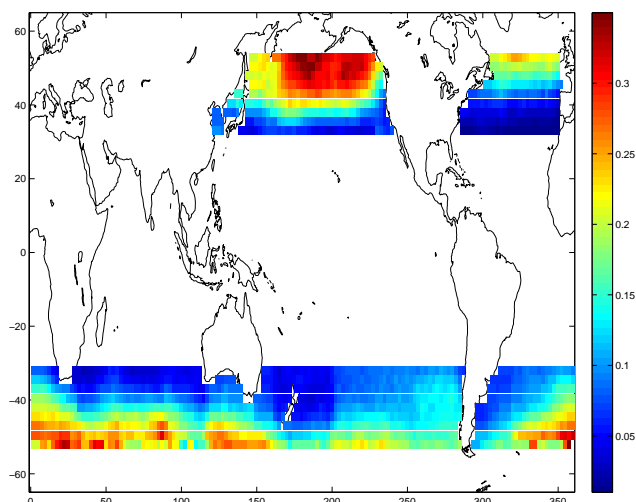
scene (Table 5). The individual impacts of cloud fraction and albedo changes on SWCRF are defined as follows.

$$\Delta SWCRF_{CF} = -\Delta f \overline{\alpha} SW\downarrow^{TOA} \tag{3}$$

$$\Delta SWCRF_{\alpha} = -\overline{f}\Delta\alpha SW\downarrow^{TOA} \tag{4}$$

where the overbar indicates the cluster average. $\Delta SWCRF_{CF}$ represents the modification in SWCRF resulting from the warm minus cold difference in cloud fraction multiplied

**Fig. 11.** JJA mean climatological spatial distribution of the frequency of Cluster 4 (Deep Altostratus).

Fig. 12. As in Fig. 11, except for Cluster 5 (Cirrus).

by the average cluster albedo and diurnal insolation, and $\Delta SWCRF_\alpha$ represents the modification in SWCRF resulting from the warm minus cold difference in albedo multiplied by average cluster cloud fraction and diurnal insolation. The fact that the sum of $\Delta SWCRF_{CF}$ and $\Delta SWCRF_\alpha$ is nearly the same as the total change in SWCRF indicates that, within a particular cloud regime, there is little correlation between variability in cloud fraction and variability in cloud albedo. All calculations are conducted such that a positive number represents a net radiative warming of the climate system for an increase in temperature.

For Cluster 1 (Small Cu), the radiative warming associated with a reduction in cloud fraction is only partially balanced by a radiative cooling associated with a small increase in albedo/optical thickness, resulting in a total SW radiative warming of $+0.7 \, \mathrm{W m^{-2} \, K^{-1}}$ (Tables 4 and 5). For Cluster 2 (Large Cu), the small radiative warming due to a decrease in cloud fraction is contrastingly more than compensated for by the radiative cooling from the increased optical thickness of these clouds (total SW radiative cooling is $-0.2 \, \mathrm{W m^{-2} \, K^{-1}}$). The reductions in cloud fraction and optical thickness with increasing temperature for Cluster 3 (Sc/St) both contribute to SW radiative warming (total is $+1.2 \, \mathrm{W m^{-2} \, K^{-1}}$). Clusters 4 and 6 (Deep As and Weak Frontal) have the greatest differences in total SW radiative cooling (-1.5 and $-1.1 \, \mathrm{W m^{-2} \, K^{-1}}$, respectively), both of which are the result of the increase in cloud optical thickness, but Cluster 7 (Strong Frontal) experiences very little change in SWCRF because its extensive and optically thick clouds are near radiative saturation. The SW radiative warming of $+0.3 \, \mathrm{W m^{-2}} \, \mathrm{K^{-1}}$ for Cluster 5 (Cirrus) primarily results from the reduction of cloud fraction, while changes in optical thickness have small impact.
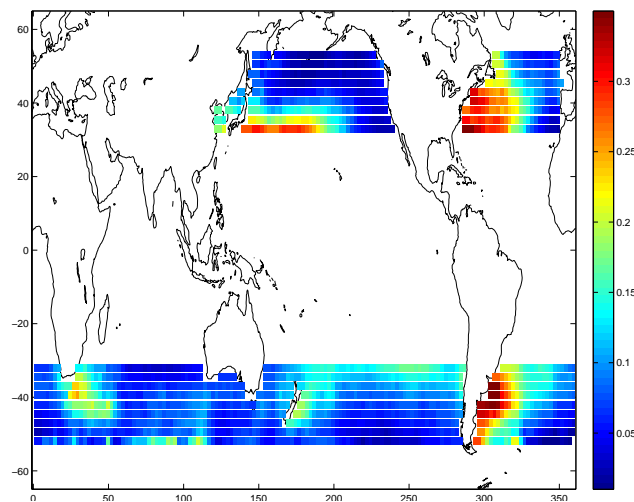
Our observational method is not a suitable analogue for the global warming scenario when calculating the difference between the average LWCRF for the warm and cold subsets. This is because tropospheric temperature differences are substantially larger than surface temperature differences in our analysis (i.e., daily temperature variability is larger for the troposphere than for the ocean surface), unlike the more uniform surface and atmospheric warming expected from a doubling of CO_2 (IPCC, 2007). Because LW emission is sensitive to temperature, our observational analysis will underestimate the upwelling LW flux from the surface relative to what will happen during future climate change and thus produce biased LWCRF. Despite our inability to quantify the total LW radiative change between warm and cold subsets, we can nonetheless examine changes in components of LWCRF, defined here as the product of cloud fraction and the difference between upwelling TOA clear-sky and overcast LW flux.

$$LWCRF = f(LW \uparrow_{\mathrm{clear}}^{\mathrm{TOA}} - LW \uparrow_{\mathrm{overcast}}^{\mathrm{TOA}}) \qquad (5)$$

Overcast LW flux is defined as follows,

$$LW \uparrow_{\mathrm{overcast}}^{\mathrm{TOA}} = (1 - g_{\mathrm{ac}})[\varepsilon \sigma T_{\mathrm{CT}}^4 + (1 - \varepsilon) LW \uparrow_{\mathrm{bc}}] \qquad (6)$$

where g_{ac} is the above-cloud greenhouse parameter, ε is the cloud emissivity, σ is the Stefan-Boltzmann constant, T_{CT} is the temperature at cloud top, and $LW \uparrow_{\mathrm{bc}}$ is the upwelling LW flux coming from beneath the cloud. Overcast refers to the flux that would occur if the entire scene were filled with clouds. We will not consider how LWCRF may be affected by changes in clear-sky LW flux in the present analysis, which has the advantage of avoiding possible disagreement between the sign of the CRF change and the sign of the cloud feedback that was noted by Soden et al. (2008).

The above-cloud greenhouse parameter accounts for the reduction in upwelling radiation that occurs between the
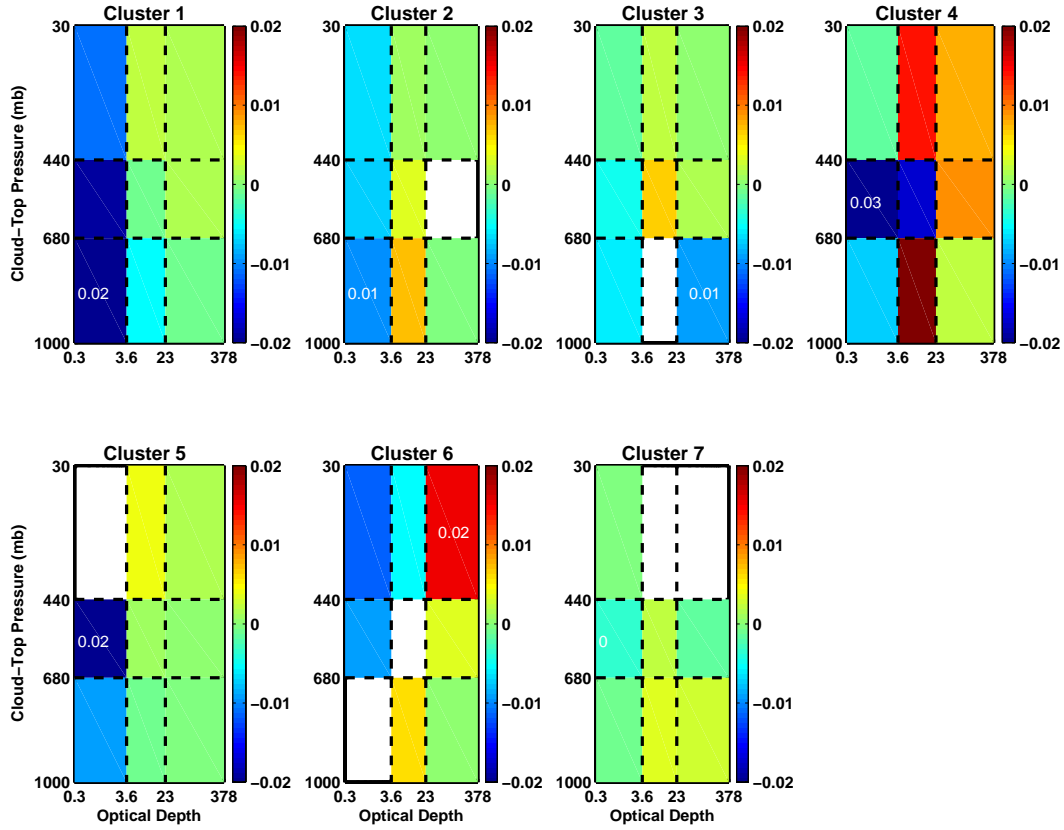
Fig. 13. ISCCP histograms of difference in cloud fraction between warm and cold subsets for each cluster.

cloud top level and the top of the atmosphere. It is similar to the greenhouse parameter devised by Raval and Ramanathan (1989) and Cess and Udelhofen (2003), except that instead of accounting for the ratio in surface and TOA LW flux, we are interested in the ratio of cloud level and TOA LW flux. The upwelling flux at cloud level is composed of thermal emission by the cloud as well as a portion of LW flux from below transmitted through the cloud. For cloud regimes that have near-unit emissivity, namely Sc/St, Deep As, Weak Frontal, and Strong Frontal, the transmission of below-cloud LW flux will be negligible. Using values of TOA overcast LW flux and T_{CT} (Table 1), we calculated average g_{ac} for those four clusters with $\varepsilon \approx 1$. Figure 18 demonstrates that g_{ac} varies nearly linearly with cloud-top pressure (i.e., inversely with atmospheric mass above the cloud top). Assuming that this is the only factor controlling g_{ac}, we interpolate the values in Fig. 18 to the average cloud-top pressures of the remaining clusters to obtain g_{ac} for those clusters with $\varepsilon < 1$. With these estimates for the fraction of upwelling radiation absorbed by the atmosphere above the cloud for each cluster, we can use Equation 6 to calculate the below-cloud LW flux for the three clusters with $\varepsilon < 1$ (Table 6).

Using cluster average values of LW flux that do not suffer from disproportionate changes in tropospheric and surface temperature, we can calculate the individual impacts of

changes in cloud fraction, cloud emissivity, and cloud-top pressure on LWCRF:

$$\Delta LWCRF_{CF} = \Delta f \overline{(LW\uparrow_{clear}^{TOA} - LW\uparrow_{overcast}^{TOA})} \quad (7)$$

$$\Delta LWCRF_{\varepsilon} = -\overline{f}(1 - \overline{g_{ac}})\Delta\varepsilon[\sigma \overline{T}_{CT}^4 - \overline{LW\uparrow_{bc}}] \quad (8)$$

$$\Delta LWCRF_{CTP} = -\overline{f}(1 - \overline{g_{ac}})[4\overline{\varepsilon}\sigma \overline{T}_{CT}^3 \overline{dT/dp} \Delta p_{CT}] \quad (9)$$

As before, the overbar indicates cluster averages and the Δ indicates the difference between warm and cold subsets. The change in cloud-top pressure Δp_{CT} was converted to a change in cloud-top temperature using cluster average lapse rate from the NCEP reanalysis. Values for $\Delta LWCRF_{CF}$, $\Delta LWCRF_{\varepsilon}$, and $\Delta LWCRF_{CTP}$ are displayed in Table 7. The consistent reduction in cloud fraction with increasing temperature across clusters results in a negative change to LWCRF, which acts as a cooling effect on the climate. Enhanced cloud emissivity (parallel to enhanced visible cloud optical thickness) with warming reduces the transmission of upwelling LW flux through those clouds with $\varepsilon < 1$ and produces a positive change in LWCRF, with the largest modification for the Cirrus regime, which is also the cluster with the smallest mean emissivity. The largest contribution to changes in LWCRF comes from shifts in cloud-top pressure.
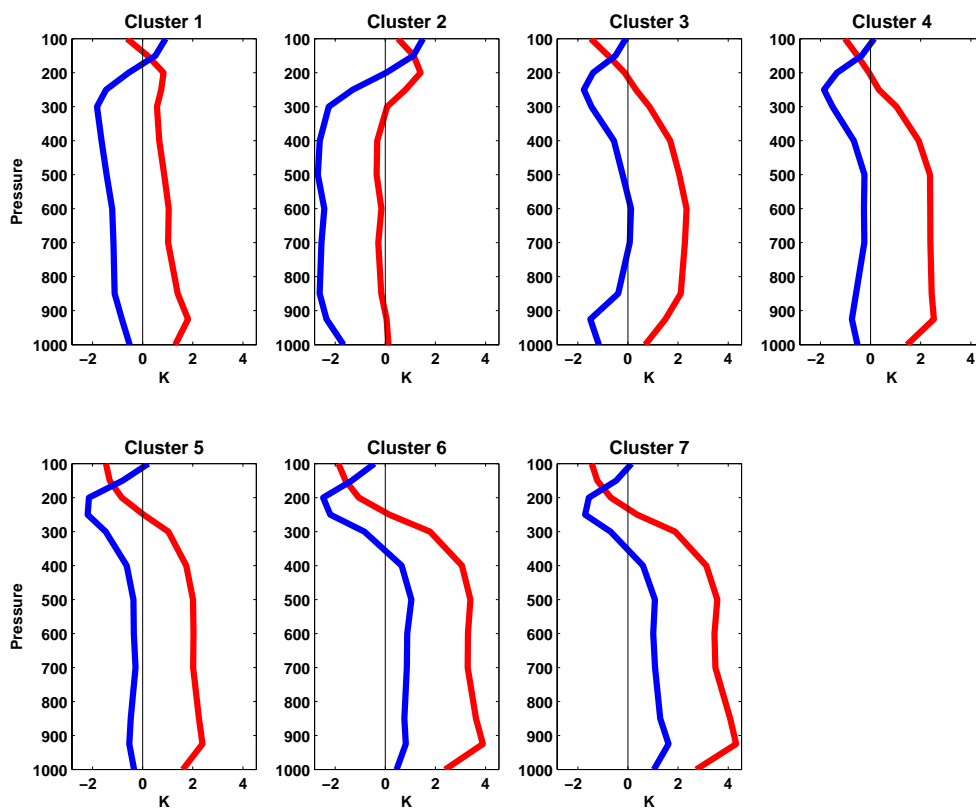
Fig. 14. Vertical profiles of temperature anomalies for warm (red) and cold (blue) subsets for each cluster from the NCEP reanalysis.

Table 6. Below-cloud upwelling LW flux.

	1 – Small Cu	2 – Large Cu	5 – Cirrus
Cluster LW$_{bc}$ (Wm^{-2})	305.0	357.7	338.0

The three low-level clusters exhibit a lowering of cloud top, leading to greater LW emission and a negative change in LWCRF, but the Cirrus cluster shows a rising cloud top, leading to less LW emission and a positive change in LWCRF.

Assuming that variations in cloud fraction, cloud emissivity, and cloud-top pressure are uncorrelated within each cluster, we can sum their individual contributions to LWCRF to obtain an approximation of the total LWCRF change associated with the difference between the warm and cold subsets. These are listed in Table 8, and indicate that the Cirrus cluster ($+1.0$ Wm^{-2} K^{-1}) has the largest positive change in LWCRF for increasing temperature, corresponding to a warming effect on the climate system. The other clusters exhibit either a weakly positive or largely negative change (near zero to -1.5 Wm^{-2} K^{-1}). For the low-level clusters, the summed LW radiative cooling values are larger than any

of the total SW radiative heating values, resulting in net radiative cooling for all low-level cloud regimes (-0.4, -0.9, and -0.3 Wm^{-2} K^{-1} for Small Cu, Large Cu, and Sc/St, respectively). The net radiative cooling for the low-level cloud regimes results from a reduction in greenhouse effect due to lower mean cloud top height and less cloud cover that is larger than the reduction in solar reflection due to less cloud cover. LW radiative changes are very small for the Deep As and Weak Frontal clusters, and SW radiative cooling due to enhanced optical thickness dominates to produce net radiative cooling for these cloud regimes (-1.1 and -1.0 Wm^{-2} K^{-1} for Deep As and Weak Frontal, respectively). LW, SW, and net radiative effects are small for the Strong Frontal cloud regime, and Cirrus is the only cloud regime for which there is both LW and SW radiative warming for increasing temperature (net value is $+1.3$ Wm^{-2} K^{-1}). The only clusters that have a change in total LWCRF that is distinct from zero at the 95% confidence level are the Large Cu and Sc/St clusters. When averaged over all clusters, weighting by frequency of cluster occurrence, the net radiative difference between warm and cold subsets is -0.5 Wm^{-2} K^{-1}; however this is not a statistically significant change.
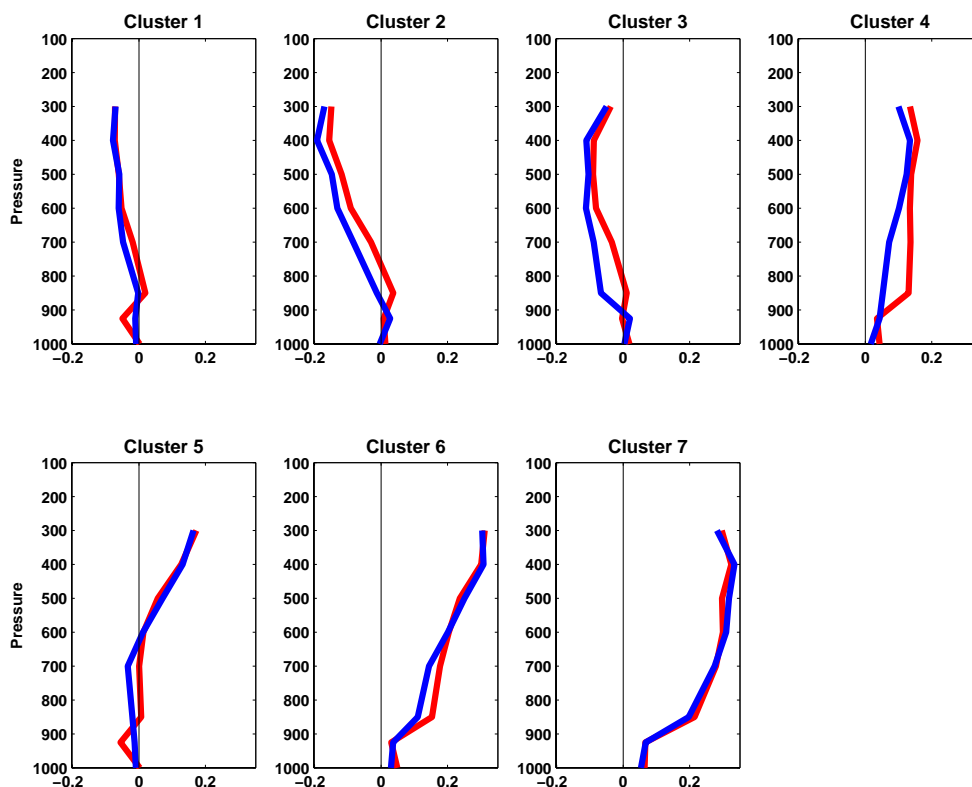
Fig. 15. As in Fig. 14, except for relative humidity anomalies.

Table 7. Average LWCRF from cloud fraction change, LWCRF from emissivity change, and LWCRF from cloud-top pressure change for the difference between the warm and cold subsets (per degree temperature change; Subsets different at the 95% confidence level are in bold).

	1 – Small Cu	2 – Large Cu	3 – Sc/St	4 – Deep As	5 – Cirrus	6 – Weak Frontal	7 – Strong Frontal
$\Delta LWCRF_{CF}$ (Wm^{-2} K^{-1})	**−0.6**	−0.1	−0.1	0.0	**−0.5**	0.0	0.0
$\Delta LWCRF_{\varepsilon}$ (Wm^{-2} K^{-1})	+0.1	**+0.3**	0.0	**+0.2**	+0.4	+0.2	0.0
$\Delta LWCRF_{CTT}$ (Wm^{-2} K^{-1})	**−0.5**	**−0.9**	**−1.4**	+0.1	+1.1	−0.1	−0.3

10 Discussion

The broad results of the preceding analysis suggest that a warmer troposphere promotes reduced cloud fraction, enhanced cloud optical thickness, a lower cloud top for low-level clouds, and a higher cloud top for cirrus over the mid-latitude ocean. Since this study was constructed to eliminate variations in temperature associated with horizontal and vertical advection along with variations in lapse rate, we presume that the observed changes are directly connected to increased temperature rather than large-scale dynamical processes. The reduction in cloud fraction with warmer temperature is consistent with the findings of previous investigations of cloud-temperature relationships over midlatitude oceans (Norris and Leovy, 1994; Weare, 1994; Norris and Iacobel-

lis, 2005; Wagner et al., 2008), but the enhancement of cloud optical thickness may not be. Williams and Webb (2009), using a clustering routine to examine the response of GCM-simulated cloud regimes to a doubling of CO_2, found that most models produced a shift towards optically thicker low-level clouds and more elevated high-level clouds with warming in the ice-free extratropics.

Theory suggests that adiabatic cloud liquid-water content will increase with temperature as a result of the increase in saturation vapor pressure, particularly at middle and high latitudes (Somerville and Remer, 1984; Betts and Harshvardhan, 1987). The conversion of ice to liquid at warmer temperature in mixed-phased clouds is also expected to enhance optical thickness at middle latitudes because cloud droplets have smaller size and fall out more slowly than ice crystals
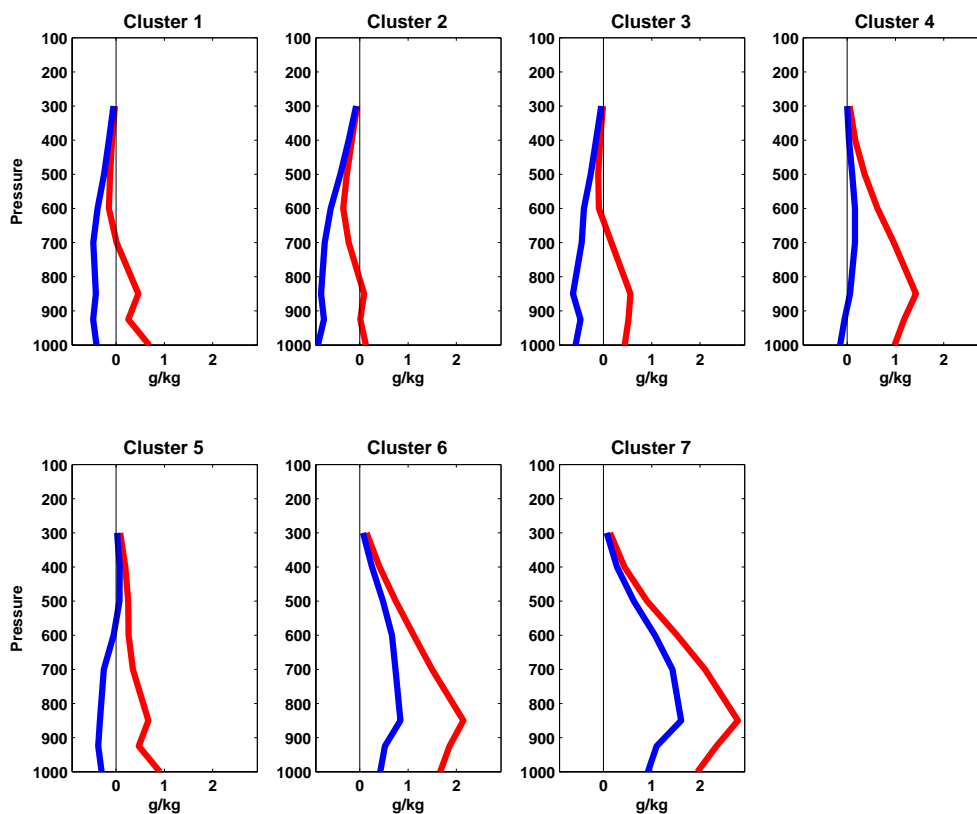
Fig. 16. As in Fig. 14, except for specific humidity anomalies.

Table 8. Total SWCRF and sum of LWCRF component changes for each cluster and the average from the midlatitude based on relative frequency of occurrence. (Subsets different at the 95% confidence level are in bold).

	1 – Small Cu	2 – Large Cu	3 – Sc/St	4 – Deep As	5 – Cirrus	6 – Weak Frontal	7 – Strong Frontal	Midlatitude Ocean Average
Cluster Frequency (%)	27.5	18.4	16.5	14.0	11.3	7.7	4.3	
Sum of LWCRF components (Wm^{-2} K^{-1})	−1.1	**−0.7**	**−1.5**	+0.3	+1.0	+0.1	−0.3	
Total SWCRF (Wm^{-2} K^{-1})	**+0.7**	−0.2	**+1.2**	**−1.5**	+0.3	−1.1	+0.1	
Net CRF (Wm^{-2} K^{-1})	−0.4	−0.9	−0.3	−1.1	+1.3	−1.0	−0.3	−0.5

(Mitchell et al., 1989). Contrastingly, previous observational work using the same satellite cloud dataset as in this study indicates that cloud optical thickness decreases with temperature over the midlatitude North Pacific (Norris and Iacobellis, 2005). Tselioudis et al. (1992) also reported a decrease in optical thickness with temperature for midlatitude oceanic low-level clouds warmer than -10°C, even when partially cloud-filled pixel effects are taken into account (Chang and Coakley, 2007). Two of the low-level cloud clusters examined in this study (Small Cu and Large Cu) exhibit an increase in op-

tical thickness with temperature, and the third cluster (Sc/St) shows a decrease smaller than that reported by Tselioudis et al. (1992). These seemingly discrepant results can be reconciled by keeping in mind that our study calculated the partial derivative of cloud properties with respect to temperature, whereas the other studies calculated the total derivative. If large-scale dynamical processes happen to reduce cloud optical thickness, while coincidently enhancing temperature, that would create a negative, rather than positive, correlation. In the case of Norris and Iacobellis (2005), it is likely that
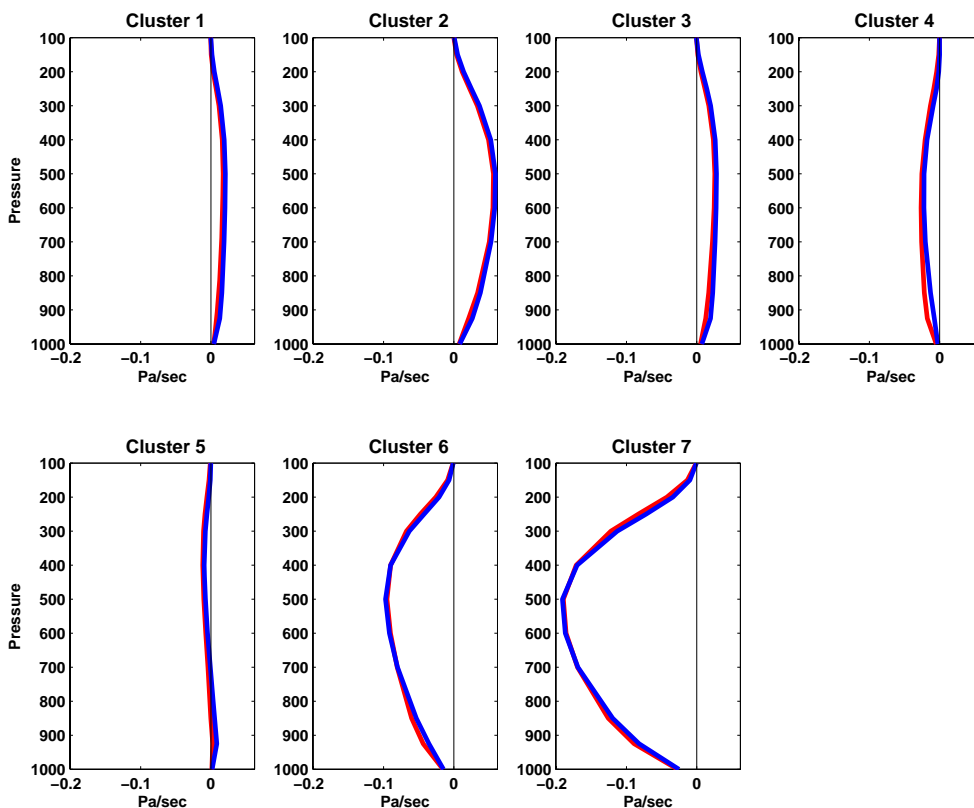
Fig. 17. As in Fig. 14, except for pressure vertical velocity profiles.

constraining vertical velocity only at 500 mb and advection only near the surface were insufficient to remove joint dynamical influences on cloudiness and temperature.

The presence of dynamical forcing may also explain why Norris and Iacobellis (2005), Chang and Coakley (2007), and Wagner et al. (2008) report that warmer temperatures are often associated with higher cloud tops, a result opposite our finding for low-level clouds. Another possibility is inaccurate or imprecise retrievals of average cloud-top pressure for a grid box with clouds at different levels.

Except for Cirrus, all cloud regimes over midlatitude oceans exhibit upwelling net radiation flux at TOA that is larger for the warm subset than for the cold subset. This result implies that, in terms of the direct response to temperature change, midlatitude oceanic clouds exert a weak negative feedback on the climate system. As the atmosphere warms due to increasing anthropogenic greenhouse gas concentrations, the increase in temperature modifies cloud properties such that more radiation goes out to space, thus mitigating the anthropogenic greenhouse radiative forcing. It is essential to keep in mind, however, that this does not mean that the total midlatitude ocean cloud feedback on the climate system is negative. Increasing temperature could also produce a change in atmospheric circulation that more strongly modifies cloud properties such that overall upwelling net

radiation flux is reduced (e.g., a positive feedback). One potential positive feedback would be a poleward shift in the storm track and associated cloudiness that moves high-albedo clouds to a latitude where there is less insolation and thus less reflection back to space (e.g., Weaver, 2003). For subtropical low-level clouds, it appears that dynamical processes play a large role in producing a positive total cloud feedback on decadal and longer time scales (Clement et al., 2009).

11 Conclusions

This study demonstrates how midlatitude oceanic clouds can be grouped into distinct regimes based on a *k*-means clustering algorithm applied to satellite-derived cloud fraction in three intervals of cloud-top pressure and three intervals of cloud optical thickness. Surface observations of cloud cover and morphological cloud type helped us interpret the radiatively based satellite cloud data and determine the vertical extent of clouds with high tops. Atmospheric dynamical and thermodynamical information, obtained from the NCEP/NCAR Reanalysis, enabled us to examine the synoptic environment and advective tendencies associated with the cloud regimes. The climatological spatial distribution and seasonal cycle of the frequencies of occurrence for each

cluster were consistent with dynamical processes generating each cloud regime.

Clusters 6 and 7 (Weak Frontal and Strong Frontal, respectively) have vertically extensive clouds with tops in the upper troposphere. They are associated with meteorological conditions indicative of being east of a trough in an upper-level synoptic wave: strong ascent, southwesterly flow, enhanced moisture throughout the troposphere, relatively warm temperature, and an elevated tropopause. These cloud regimes are climatologically most frequent in storm track regions and preferentially occur during the winter season. The low-level cloud clusters (1 – Small Cu, 2 – Large Cu, and 3 – Sc/St) are associated with weak descent, a dry upper troposphere, and relatively cool and dry horizontal advective tendencies, consistent with the expected dynamical conditions that would be associated with low-level clouds over the ocean. Cluster 2 (Large Cu) is climatologically most frequent during winter and occurs with a relatively cold temperature throughout the troposphere. In contrast, Cluster 3 (Sc/St) is climatologically most frequent during summer and occurs with a temperature inversion under a relatively warm free troposphere. Cluster 1 (Small Cu) is climatologically most frequent equatorward of $40°$ and exhibits little seasonal cycle. One of the remaining clusters, 5 – Cirrus, is most common east of continents and occurs with a dry lower troposphere and a moist upper troposphere produced by horizontal advective moistening and weak ascent. The last cluster, 4 – Deep As, is the only cloud regime with a top in the middle troposphere. It is most common poleward of $50°$ and resembles the frontal clusters, albeit with substantially smaller magnitude.

Each of these relatively homogeneous clusters was divided into a warm subset and cold subset according to tropospheric temperature anomalies with uniform sampling over grid boxes and calendar months. For each cluster, we constrained vertical and horizontal temperature advection to have near-median values at three different levels in the troposphere, and we constrained lapse rate to have near-median values in the lower troposphere and in the tropopause region. This enabled us to isolate changes in cloud properties as a direct response to increasing temperature, as opposed to changes in cloud properties from dynamical forcing, which also happened to be associated with a change in temperature.

Negligible change in cloud fraction is seen for the Deep As and two Frontal regimes, but for the rest of the clusters, the warm subset consistently exhibits less cloud fraction than the cold subset. No change in optical depth is seen for the Strong Frontal regime, but for all of the other clusters except for Sc/St, the warm subset consistently has greater optical depth than the cold subset. The changes in cloud-top pressure are less consistent, with the three low-level clusters (Small Cu, Large Cu, and Sc/St) showing greater cloud-top pressure for the warm subset and the Cirrus cluster showing greater cloud-top pressure for the cold subset. We then used ISCCP flux data to examine how these changes in cloud properties with increasing temperature affected upwelling SW and LW
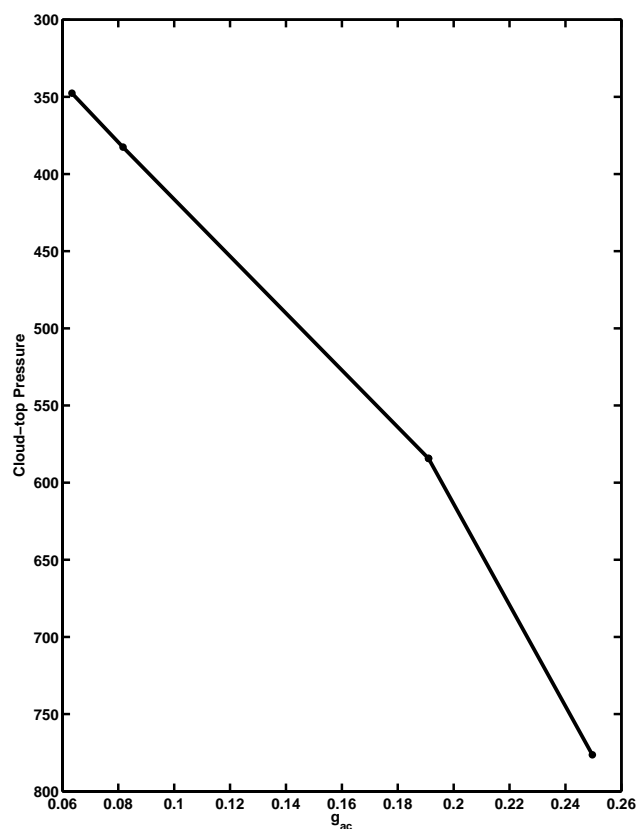

Fig. 18. Relationship between the above-cloud greenhouse parameter and cloud-top pressure.

radiative flux at the top of the atmosphere. The reduction of cloud fraction at warmer temperature allows more SW radiation to be absorbed by the Earth, but this is partially or wholly canceled by less absorption of outgoing LW radiation. The enhancement of optical thickness at warmer temperature increases the reflection of SW radiation back to space, although this is partially canceled by less transmission of LW radiation through clouds for those cloud regimes with emissivity less than zero (Small Cu, Large Cu, and Cirrus). The decrease in cloud-top height at warmer temperature for the low-level clusters increases LW emission by the clouds, and the increase in cloud-top height for Cirrus decreases LW emission. Net upwelling radiation increases at warmer temperature for every cluster except Cirrus.

Averaged over all clusters, with weighting by frequency of occurrence, the increase in upwelling flux is about $0.5 \, \mathrm{Wm}^{-2} \, \mathrm{K}^{-1}$, implying that the direct response of midlatitude oceanic clouds to warmer temperature acts as a negative feedback on the climate system (e.g., partially canceling the reduction in upwelling LW flux caused by increasing greenhouse gas concentrations). This result, however, does not mean that the total cloud feedback by midlatitude oceanic clouds is negative. A change in atmospheric mean circulation and variability caused by anthropogenic greenhouse warming could

modify the dynamical forcing of clouds in a manner that overwhelms the temperature response and generates a positive feedback. For example, a poleward shift of the storm tracks could reduce the radiative cooling effect of the weak and strong frontal cloud regimes. More research is needed to determine what changes in atmospheric dynamics are likely to accompany climate change. The cloud-temperature dynamical relationships revealed in this study could provide a useful diagnostic tool for the evaluation of global climate models.

Appendix A

Charlock and Ramanathan et al. (1985) defined cloud radiative forcing as the difference in the radiative flux between all-sky conditions and cloud-free conditions at the top of the atmosphere (TOA), for both shortwave (SWCRF) and longwave radiation (LWCRF):

$$SWCRF = (SW \uparrow_{clear}^{TOA} - SW \uparrow_{all-sky}^{TOA}) \tag{A1}$$

$$LWCRF = (LW \uparrow_{clear}^{TOA} - LW \uparrow_{all-sky}^{TOA}) \tag{A2}$$

Here, SW and LW refer respectively to the shortwave and longwave flux of radiation for either clear or all-sky conditions. For this equation, we are only interested in the up-welling component of the radiative flux. The ISCCP cloud data we used are from the three-hourly observation closest to local noon, the time of day when downwelling shortwave radiation at TOA and the upwelling longwave radiation at the surface are diurnal maximums and have large variability over season and location. In order to avoid a radiative weighting that would bias towards summertime and low-latitude points, we normalize our radiation parameters by the downwelling SW at TOA for SWCRF and by the upwelling LW radiation at the surface. Thus our cloud radiative forcing parameters become:

$$SWCRF_{norm} = (SW \uparrow_{clear}^{TOA} - SW \uparrow_{all-sky}^{TOA})/(SW \downarrow_{TOA}) \tag{A3}$$

$$LWCRF_{norm} = (LW \uparrow_{clear}^{TOA} - LW \uparrow_{all-sky}^{TOA})/(LW \uparrow_{surface}) \tag{A4}$$

To get a diurnal average of the cloud forcing in units of Wm^2, as opposed to a noontime value, we multiplied the normalized cloud forcing by the diurnally averaged value of downwelling shortwave flux at TOA for SWCRF$_{norm}$ or the upwelling longwave flux at the surface for LWCRF$_{norm}$. Both of these values were determined by averaging the ISCCP flux data for all three-hourly data points during a day, yielding:

$$SWCRF_{diurnal} = SW \downarrow_{diurnal}^{TOA}$$
$$(SW \uparrow_{clear}^{TOA} - SW \uparrow_{all-sky}^{TOA})/SW \downarrow_{TOA} \tag{A5}$$

$$LWCRF_{diurnal} = LW \uparrow_{diurnal}^{surface}$$
$$(LW \uparrow_{clear}^{TOA} - LW \uparrow_{all-sky}^{TOA})/LW \uparrow^{surface} \tag{A6}$$

To avoid giving more radiative weighting to cloud changes that occur at lower latitudes and during the summer season, we separately averaged SWCRF$_{norm}$ and LWCRF$_{norm}$ over all grid boxes and seasons before multiplying them by diurnal mean SW and LW separately averaged over all grid boxes and seasons. Our results are qualitatively the same irrespective of radiative weighting.

References

Betts, A. K. and Harshvardhan: Thermodynamic constraint on the cloud liquid water feedback in climate models, J. Geophys. Res., 92, 8483–8485, 1987.

Bony, S., Dufresne, J.-L., Le Treut, H., Morcrette, J.-J., and Senior, C.: On dynamic and thermodynamic components of cloud changes, Clim. Dyn., 22, 71–86, 2004.

Cess, R. D. and Udelhofen, P. M.: Climate change during 1985–1999: cloud interactions determined from satellite measurements, Geophys. Res. Lett., 30, 1019, doi:10.1029/2002GL016128, 2003.

Chang, F.-L. and Coakley, J. A.: Relationships between marine stratus cloud optical depth and temperature: Inferences from AVHRR observations, J. Climate, 20, 2022–2036, 2007.

Charlock, T. P. and Ramanathan, V.: The Albedo Field and Cloud Radiative Forcing Produced by a General Circulation Model with Internally Generated Cloud Optics, J. Atmos. Sci., 42, 1408–1429, 1985.

Clement, A. C., Burgman, R., and Norris, J. R.: Observational and model evidence for positive low-level cloud feedback, Science, 325, 460–426, 2009.

Gordon, N. D., Norris, J. R., Weaver, C. P., and Klein, S. A.: Cluster analysis of cloud regimes and characteristic dynamics of midlatitude synoptic systems in observations and a model, J. Geophys. Res., 110, D15S17, doi:10.1029/2004JD005027, 2005.

Hahn, C. J. and Warren, S. G.: Extended Edited Cloud Reports from Ships and Land Stations over the Globe, 1952–1996, Numerical Data Package NDP-026C, Carbon Dioxide Information Analysis Center (CDIAC), Department of Energy, Oak Ridge, Tennessee (79 pp.), 1999.

Hartigan, J. A.: Clustering Algorithms, Wiley Press, New York, NY, 351 pp., 1975.5

IPCC Climate Change 2007: The Physical Science Basis. Contribution of Working Group I to the Fourth Assessment Report of the Intergovernmental Panel on Climate Change edited by: Solomon, S., Qin, D., Manning, M., Chen, Z., Marquis, M., Averyt, K. B., Tignor, M., and Miller, H. L., Cambridge University Press, Cambridge, United Kingdom and New York, NY, USA, 996 pp., 2007.

Jakob, C.: An improved strategy for the evaluation of cloud parameterizations in GCMs, B. Am. Meteor. Soc., 84, 1387–1401, 2003.

Jakob, C. and G. Tselioudis: Objective Identification of Cloud Regimes in the Tropical West Pacific, Geophys. Res. Lett., 30(21), 2082, doi:10.1029/2003GL018367, 2003.

Jakob, C., Tselioudis, G., and Hume, T.: The radiative, cloud and thermodynamic properties of the major Tropical Western Pacific cloud regimes, J. Climate, 18, 1203–1215, 2005.

Kalnay E., Kanamitsu, M., Kistler, R., Collins, W., Deaven, D., Gandin, L., Iredell, M., Saha, S., White, G., Woollen, J., Zhu, Y., Chelliah, M., Ebisuzaki, W., Higgins, W., Janowiak, J., Mo, K. C., Ropelewski, C., Wang, J., Leetmaa, A., Reynolds, R., Jenne, R., and Joseph, D.: The NCEP/NCAR 40-year reanalysis project, B. Am. Meteor. Soc., 77, 437–470, 1996.

Klein, S. A., and Jakob, C.: Validation and sensitivities of frontal clouds simulated by the ECMWF model, Mon. Wea. Rev., **127**, 2514-2531, 1999.

Lau, N.-C. and Crane, M. W.: A satellite view of the synoptic-scale organization of cloud cover in midlatitude and tropical circulation systems, Mon. Wea. Rev., 123, 1984–2006, 1995.

Mitchell, J. F. B., Senior, C. A., and Ingram, W. J.: CO_2 and climate: a missing feedback?, Nature, 341, 132–134, 1989.

Norris, J. R.: Low cloud type over the ocean from surface observations. Part I: relationship to surface meteorology and the vertical distribution of temperature and moisture, J. Climate, 11, 369–382, 1998a.

Norris, J. R.: Low cloud type over the ocean from surface observations. Part II: geographical and seasonal variations, J. Climate, 11, 383–403, 1998b.

Norris, J. R. and Leovy, C. B.: Interannual variability in stratiform cloudiness and sea surface temperature, J. Climate, 7, 1915–1925, 1994.

Norris, J. R. and Klein, S. A.: Low cloud type over the ocean from surface observations. Part III: relationship to vertical motion and the regional surface synoptic environment, J. Climate, 13, 245–256, 2000.

Norris, J. R. and Weaver, C. P.: Improved Techniques for Evaluating GCM Cloudiness Applied to the NCAR CCM3, J. Climate, 14, 2540–2550, 2001.

Norris, J. R. and Iacobellis, S. F.: North Pacific cloud feedbacks inferred from synoptic-scale dynamic and thermodynamic relationships, J. Climate, 18, 4862–4878, 2005.

Ramanathan, V., Barkstrom, B. R., and Harrison, E. F.: Climate and the Earth's Radiation Budget, Physics Today, 42(5), 22–33, 1989.

Raval, A. and Ramanathan, V.: Observational determination of the greenhouse effect, Nature, 342, 758–761, 1989.

Ringer, M. A., McAvaney, B. J., Andronova, N., Buja, L. E., Esch, M., Ingram, W. J., Li, B., Quaas, J., Roeckner, E., Senior, C. A., Soden, B. J., Volodin, E. M., Webb, M. J., and Williams, K. D.: Global mean cloud feedbacks in idealized climate change experiments, Geophys. Res. Lett., 33(7), L07718, doi:10.1029/2005GL025370, 2006.

Rossow, W. B. and Garder, L. C.: Validation of ISCCP cloud detections, J. Climate, 6, 2370–2393, 1993.

Rossow, W. B., Walker, A. W., Beuschel, D. E., and Roiter, M. D.: International Satellite Cloud Climatology Project (ISCCP) Documentation of New Cloud Datasets, WMO/TD-No. 737, World Meteorological Organization, 115 pp., 1996.

Rossow, W. B. and Schiffer, R. A.: Advances in Understanding ISCCP, B. Am. Meteor. Soc., 80, 2261–2287, 1999.

Rossow, W. B., Tselioudis, G., Polak, A., and Jakob, C.: Tropical climate described as a distribution of weather states indicated by distinct mesoscale cloud property mixtures, Geophys. Res. Lett., 32, L21812, doi:10.1029/2005GL024584, 2005.

Soden, B. J., Held, I. M., Colman, R., Shell, K. M., Kiehl, J. T., and Shields, C. A.: Quantifying climate feedbacks using radiative kernels, J. Climate, 21, 3504–3520, 2008.

Somerville, R. C. J. and Remer, L. A.: Cloud optical thickness feedbacks in the CO2 climate problem, J. Geophys. Res., 89, 9668–9672, 1984.

Tselioudis, G. and Jakob, C.: Evaluation of midlatitude cloud properties in a weather and a climate model: dependence on dynamic regime and spatial resolution, J. Geophys. Res., 107, 4781, doi:10.1029/2002JD002259, 2002.

Wagner, T., Beirle, S., Deutschmann, T., Grzegorski, M., and Platt, U.: Dependence of cloud properties derived from spectrally resolved visible satellite observations on surface temperature, Atmos. Chem. Phys., 8, 2299–2312, doi:10.5194/acp-8-2299-2008, 2008.

Weaver, C. P.: Efficiency of storm tracks an important climate parameter? The role of cloud radiative forcing in poleward heat transport, J. Geophys. Res., 108, 4018, doi:10.1029/2002JD002756, 2003.

Weaver, C. P. and Ramanathan, V.: The link between summertime cloud radiative forcing and extratropical cyclones in the N. Pacific, J. Climate, 9, 2093–2109, 1996.

Weaver, C. P. and Ramanathan, V.: Relationships between large-scale vertical velocity, static stability, and cloud radiative forcing over Northern Hemisphere extratropical oceans, J. Climate, 10, 2871–2887, 1997.

Williams K. D. and Tselioudis, G.: GCM intercomparison of global cloud regimes: Present-day evaluation and climate change response, Clim. Dyn., 29(2–3), doi:10.1007/s00382-007-0232-2, 2007.

Williams, K. D. and Webb, M. J.: A quantitative performance assessment of cloud regimes in climate models, Clim. Dyn., 33(1), doi:10.1007/s00382-008-0443-1, 2009.

Zhang, Y., Rossow, W. B., Lacis, A. A., Oinas, V., and Mishchenko, M. I.: Calculation of radiative fluxes from the surface to top of atmosphere based on ISCCP and other global data sets: Refinements of the radiative transfer model and the input data, J. Geophys. Res., 109, D19105, doi:10.1029/2003JD004457, 2004.